Multimodal Mapping of Electrical and Mechanical Latency of Human-Induced Pluripotent Stem Cell-Derived Cardiomyocyte Layers

ACSNANO

www.acsnano.org

ARTICLE

Multimodal Mapping of Electrical and Mechanical Latency of Human-Induced Pluripotent Stem Cell-Derived Cardiomyocyte Layers

Xinyu Zhang, Margherita Burattini, Jens Duru, Nafsika Chala, Nino Wyssen, "Carla Cofino Fabres, Jose Manuel Rivera Arbelaez, Robert Passier, Dimos Poulikakos, Aldo Ferrari, Christina Tringides, János Vörös, Giovanni Battista Luciani, Michele Miragoli,* and Tomaso Zambelli*

Cite This: https://doi.org/10.1021/acsnano.4c03896 Read Online

ACCESS | Metrics & More | Article Recommendations | Supporting Information

ABSTRACT: The synchronization of the electrical and mechanical coupling assures the physiological pump function of the heart, but life-threatening pathologies may jeopardize this equilibrium. Recently, human induced pluripotent stem cell-derived cardiomyocytes (hiPSC-CMs) have emerged as a model for personalized investigation because they can recapitulate human diseased traits, such as compromised electrical capacity or mechanical circuit disruption. This research avails the model of hiPSC-CMs and showcases innovative techniques to study the electrical and mechanical properties as well as their modulation due to inherited cardiomyopathies. In this work, hiPSC-CMs carrying either Brugada syndrome (BRU) or dilated cardiomyopathy (DCM), were organized in a bilayer configuration to first validate the experimental methods and second mimic the physiological environment. High-density CMOS-based microelectrode arrays (HD-MEA) have been employed to study the electrical activity. Furthermore, mechanical function was investigated via quantitative video-based evaluation, upon stimulation with a β-adrenergic agonist. This study introduces two experimental methods. First, high-throughput mechanical measurements in the hiPSC-CM layers (xy-inspection) are obtained using both a recently developed optical tracker (OPT) and confocal reference-free traction force microscopy (cTFM) aimed to quantify cardiac kinematics. Second, atomic force microscopy (AFM) with FluidFM probes, combined with the xy-inspection methods, supplemented a three-dimensional understanding of cell−cell mechanical coupling (xyz-inspection). This particular combination represents a multi-technique approach to detecting electrical and mechanical latency among the cell layers, examining differences and possible implications following inherited cardiomyopathies. It can not only detect disease characteristics in the proposed in vitro model but also quantitatively assess its response to drugs, thereby demonstrating its feasibility as a scalable tool for clinical and pharmacological studies.

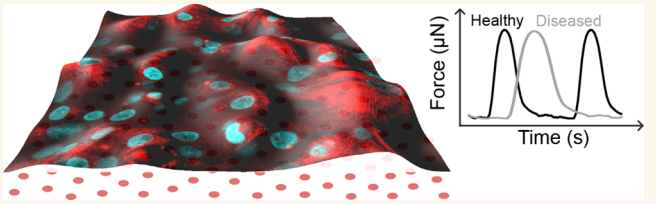

KEYWORDS: *hiPSC-CMs, Brugada syndrome, dilated cardiomyopathy, traction force microscopy, optical tracker, HD-MEA*

INTRODUCTION

Cardiovascular diseases continue to be a predominant cause of illness and mortality worldwide, using estimates from 204 countries and territories from 1990 to 2019.[1] Cardiomyocytes (CMs) are the functional building blocks of the heart and play a central role in cardiac contraction.[2,3] Their ability to ensure coordinated contraction at the tissue level is based on highly coupled electrical and mechanical signaling, resulting in rhythmic cardiac activity.[4,5] Any disruption in this coupling, whether due to electrical (i.e., arrhythmia, conduction block by defected ion channels (Brugada syndrome))[6−8] or mechanical disturbances (dilated cardiomyopathy,[9,10] myocardial infarction[11]), can lead to potentially life-threatening conditions.[12,13]

Coordinated contraction begins with the transmission of electrical signals between individual CMs through key

Received: March 22, 2024
Revised: July 23, 2024
Accepted: July 29, 2024

conduction pathways such as gap junctions.[14] Afterward, the electrical signal is converted to a mechanical contraction through a chain of biochemical cues for each CMs, known as electro-mechanical coupling.[5] Under the regulation of electrical activity, mechanical forces appear between neighboring CMs, as well as between CMs and the extracellular matrix (ECM). Mechanical crosstalk is especially complex in CMs, as CMs sense and generate forces at the same time, this interaction between CMs and external forces is bidirectional and occurs through complex biochemical signaling pathways.[15] For example, between CMs, intercalated discs are the highway through which electrical and mechanical signals flow,[16,17] and transmembrane proteins (e.g., desmosomes, N-cadherin) mechanically link the cytoskeleton of two adjacent CMs.[16,18] The resulting force between adjacent cells is correlated with the size of these junctions, as previous studies have shown.[19] Communication between the cell and the ECM is mainly through focal adhesions involving macromolecular assemblies (such as integrins and receptors), which link intracellular actin and the ECM.[20,21] Irregularities in this machinery can occur and cause severe cardiac pathologies.[12,13]

The elucidation of coordinated CMs contraction and cardiovascular disease mechanisms relies on functional studies with in vivo animal models and in vitro models. Animal models have become increasingly restricted for ethical reasons[22] and do not completely recapitulate the human geno- and phenotype. In contrast, in vitro models, particularly human-induced pluripotent stem cell-derived cardiomyocytes (hiPSC-CMs), offer an alternative approach to animal cell models.[23] The application of hiPSC-CMs also provides a particular advantage in modeling cardiac diseases, they can be engineered or patient-derived disease lines,[23] providing information on cardiac diseases and variability of drug toxicity for personalized medicine.[24−26] In this study, we employed hiPSC-CMs in a bilayer configuration as our in vitro model, which is considered more physiologically relevant compared to the single-cell studies.[3] Despite its relevance, the cell−cell interaction of this configuration still lacks in-depth studies.[27] This knowledge gap may arise due to the complex machinery of CM contraction mentioned above, involving interactions that occur between mechanical, electrical, and biochemical cues.[15] The in vitro model adopted in this work not only allows the study of contractility differences in healthy and diseased hiPSC-CMs both mechanically and electrically but also offers a considerable opportunity to investigate the interaction between hiPSC-CMs.

In achieving clinical relevance for pharmaceutical analysis, in addition to a carefully designed in vitro model, a validated quantification of CM contraction is also of great importance. This quantification has to address two aspects of the CM contraction measurement: the electrical action potential and mechanical contractility.

Electrical quantification typically relies on established electrophysiological techniques, such as patch clamps or glass microelectrode arrays (MEAs).[28,29] Although the patch clamp generally provides information about the action potential of individual CMs, it lacks the ability to evaluate the overall electrical signal propagation within the bilayer model adopted with single-cell resolution. Recently, high-throughput electrophysiology techniques, such as glass-based or complementary metal-oxide semiconductors (CMOS)-based multielectrode arrays (MEAs) showed potential in measuring the electrical connectivity of CMs.[30] Glass MEAs provide spatial information on the action potentials of a layer of CMs, but the recorded activity is typically the collective electrical signals of surrounding cells.[28,31] In this work, we used a high-density CMOS-based microelectrode array (HD-MEA) platform to enable the recording of extracellular action potentials (ecAP) at the cellular level with a spatial resolution of 17.5 μm, corresponding to the pitch between electrodes, and a temporal resolution of 0.05 ms (Figure 1).[32−34]

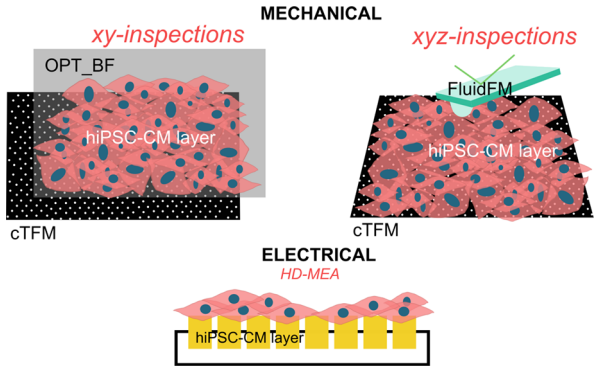

Figure 1. Experimental methods to quantify the mechanical and electrical behavior of a hiPSC-CM bilayer. Mechanical quantification of the hiPSC-CM layer is separately performed with two methods: xy-inspection focuses on high throughput force analysis in the *xy* axis (from QD: while focusing on the basal side) with simultaneous recording of bright field (BF); xyz-inspection provides force recording of *xy* (from QD focusing on the basal side analyzed by cTFM), and *z* (from FluidFM focusing on the apical side). Electrically, the HD-MEA platform is used to record the action potential map (yellow pitch indicates the CMOS recording electrodes).

As the other part of the equation, mechanical machinery can be analyzed by using different approaches. Traction force microscopy (TFM) has been instrumental in mapping contractile forces generated by cells.[35−38] Among various TFM techniques, particle tracking is widely used, providing high spatial resolution with hundreds of nanometers data with pN sensitivity, but it requires a reference image and lacks tunable lateral resolution for complex cellular systems,[35,39] limiting its use to the single cell level.[40] Video microscopy-based TFM techniques are often employed for the evaluation of contractility of in vitro tissue models with multiple cell types or 3D CM spheroids,[41,42]overcoming the limitations of particle tracking TFM. Despite their great potential for automation, video microscopy-based methods normally measure displacement in the range of microns, failing to evaluate the μN force developed by the sample. Thus, to match the displacement with the force measurements, calibration is needed.[42] Confocal reference-free Traction Force Microscopy (cTFM) is capable of measuring the contractility of CMs layer[27,43,44] with a high-resolution characteristic.[45] Specifically, it achieves tunable lateral resolution through adjustable spacing in the array and obtains accurate measurements without the need for a reference image. In this work, we calibrated a recently developed video microscopy method: Optical Tracker (OPT) with cTFM (Figure 1, Video S1). Combining them allowed us to measure the contractility of hiPSC-CM layers in 2D (xy inspection, Figure 1). Furthermore, FluidFM was enforced to inspect and complement the xy inspection with vertical displacement[46,47] (xyz inspection Figure 1).

https://doi.org/10.1021/acsnano.4c03896
ACS Nano XXXX, XXX, XXX−XXX

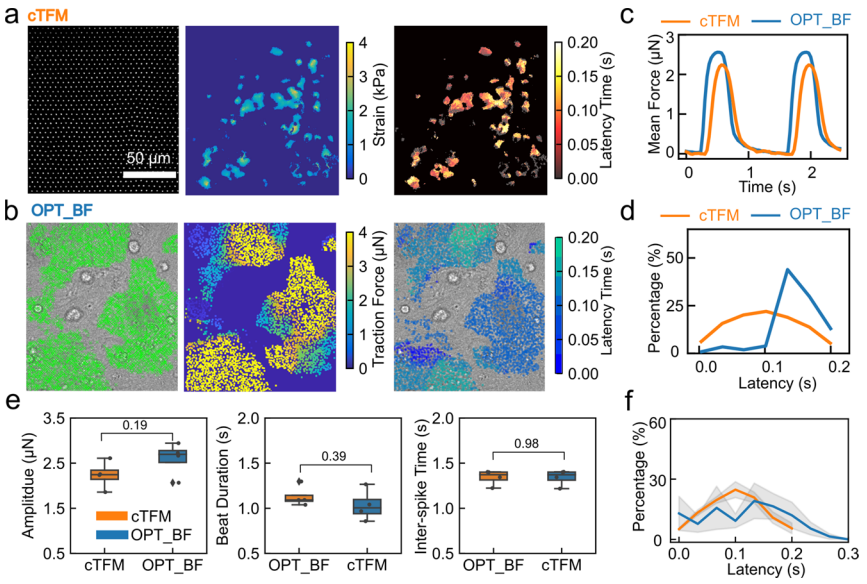

Figure 2. Mechanical properties of hiPSC-CMs with xy- inspection. (a) cTFM analyzes the deformation of a quantum dot array with a spacing of 5 μm (first panel) and generates the corresponding strain map induced by the contractile forces of hiPSC-CMs (second panel). The latency is mapped spatially (third panel). (b) BF channel of recording could be analyzed by OPT_BF (first panel) with detected moving features indicated in green crosses, yielding the corresponding force map (second panel) and latency map (third panel). (c) Mean traction force profiles of corresponding methods and cTFM (orange) are compared with those of the OPTBF (blue). (d) Latency distributions of corresponding latency map in panels a and b are displayed for cTFM (orange) and OPTBF (blue). (e) A statistical comparison of contraction features (amplitude, beat duration, and interspike time) between OPT_BF and cTFM (N = 4). No statistically significant difference between any measured parameters. (f) Latency distributions were integrated with different samples (N = 4), see details in methods TFM analysis section.

The cTFM technique utilizes quantum dots (CdSe) with 25 nm size,[48] deposited with the nanodrip platform having 100−200 nm spatial resolution, while HD-MEA chips, recording ecAP of hiPSC-CMs, are fabricated according to a lithography process with 180 nm resolution. Additionally, the QD array is detected with 400 nm/pixel resolution in the xy-inspection, while the xyz-inspection provides a 100 nm/pixel resolution, enabling FluidFM measurements of the hiPSC-CMs contractility in the z direction with pN sensitivity.

The objective of this study was to quantitatively characterize the hiPSC-CM bilayer electrically and mechanically using the presented platforms. Moreover, with the provided lateral resolution, we inferred further information about local effects; particularly, we were able to measure and define the time difference between the contraction peak of each pixel within the layer, which we here refer to as the "latency" of the hiPSC-CM contraction. Mechanically, the latency of CMs has rarely been studied due to the lack of spatial resolution.[49] Electrically, HD-MEA technology allowed the study of ecAP propagation between CMs at cell−cell resolution, which is still missing in the literature[28](Figure 1, Video S2). The quantification of the overall contractility and the latency distribution were efficiently estimated and further validated to differentiate healthy hiPSC-CM with pathology (Brugada syndrome and dilated cardiomyopathy) and applied to measure the corresponding drug response of diseased hiPSC-CMs (isoproterenol).

RESULTS AND DISCUSSION

The xy-Inspection Methodology and the Latency. For a better representation of the tissue function, we considered a layered hiPSC-CMs construct, as it reflects the physiological state of hiPSC-CMs with rhythmic contraction. This configuration also contains abundant connections between cell layers (cell−cell) and with the substrate (cell-ECM). These multidimensional cell−cell and cell-ECM interactions lead to varying contractions at each hiPSC-CM. The intricate kinetics and synchronization inherent to interacting cells are challenging to quantify and constitute the primary focus of our investigation.[28,50] Mechanically, we combined two methods: video-microscopy based optical tracker (OPT), and traction force microscopy (cTFM)[45] to measure the contractility in planar force in x and y of layered hiPSC-CMs.

In the cTFM technique, the strain exerted by the cells induces a deformation of the elastomer and subsequent displacement of quantum dots (QDs), which were previously deposited on the elastomer in the form of hexagonal arrays (Figure 2 a first panel, Video S1) (for further details, please refer to the experimental section, cTFM substrate fabrication). The shape distortion of the QD array from the relaxed state allows for calculating the active traction being exerted by the cells onto the substrate with the help of a finite element method algorithm (FEM).[51] By changing the spacing between QDs during the printing process, the cTFM lateral sensitivity can be tuned for single cells and a cell layer. Here, we used arrays with 5 μm spacing as a good compromise between lateral resolution and sensitivity, since noise from printing error increases with smaller spacing. Moreover, since the elastomer is transparent, concurrent imaging with a confocal laser scanning microscope (CLSM) was possible. The bright field (BF) transmitted-light channel was used for the OPT measurement of the beating hiPSC-CM layer (OPT_BF, Figure 2b, first panel, Video S1). OPT_BF extracted the moving features using the Kanade-Lucas-Tomasi (KLT) algorithm (Figure S2, see details in experimental: OPT_BF Data Analysis section).[52−54] Concurrently, the hiPSC-CM displacement on the elastomer was tracked over time in the BF

https://doi.org/10.1021/acsnano.4c03896
ACS Nano XXXX, XXX, XXX−XXX

(Figure 2b second panel). The displacements were transformed with the Boussinesq equation[55,56] into μN force. OPT_BF, as it was recently developed, lacks experimental validation, and while cTFM is a well-established TFM method, its application at the tissue level is lacking. Therefore, we validated OPT and cTFM with each other in evaluating the same contraction events of layered hiPSC-CMs.

To ensure faithful quantification of the mechanical contraction of the cells within hiPSC-CM layers, we carefully optimized the mechanical platforms separately. First, cTFM was used to generate a corresponding traction map illustrating the force change over the course of a hiPSC-CMs beat. The traction strain map is a quantitative representation of strain magnitudes within the *xy* plane in 2D (Figure 2a, second panel) (See details in experimental: cTFM Data Analysis section). These values are typically expressed in kilo-Pascals (kPa)[57] and can be multiplied by the area of each pixel to obtain information about the local deformation forces. To compare forces between different samples, it is necessary to extract the mean force of a strain map. In order to obtain a mean force that is characteristic of the contractile cells, we need to eliminate inevitable differences in active cell coverage. Therefore, a mask was determined based on the map of hiPSC-CMs at rest and in a contracted state, selecting only the "active" pixels. Superimposing this mask on the traction force map, the contraction was quantified much more precisely, enabling the comparison of force changes over time between different samples (details in Figure S1 and experimental: cTFM Data Analysis section). Second, OPT_BF was tested against variations in brightness, yielding a stable detection of force regardless of the image parameter changes (Figure S2.a,b), eliminating this common problem of video micros-copy.[42,58] By extracting the mean from all of the pixels of the masked strain map in cTFM and plotting it over time, a force profile was generated from cTFM strain maps. Simultaneously, the root-mean-square (RMS) and the mean of the force from all pixels of the moving features ("active pixels") detected in the OPT_BF force map can also be plotted over time (Figure S2.c). Since the RMS provides a more accurate representation of the overall magnitude of forces, it was chosen to be the comparable average force for each image. The force profiles over time measured by both methods represented the overall beating of the hiPSC-CMs bilayer within the field of view (normally 200 × 200 μm^2) (Figures 2c and S1.b,c).

After the initial calibration, we investigated further the temporal dynamics of the hiPSC-CM contraction, taking advantage of the lateral resolution of both methods. Every pixel in the strain/force map exhibited periodic amplitude changes over time, reflecting the rhythmic beating of the hiPSC-CMs. Exemplified with cTFM, these individual force profiles were further analyzed using a peak detection function, generating a distribution of key parameters: peak time points, peak amplitudes, beat duration, and interspike time (Figure S1.d). These parameters are indicators of the sample status and can also be considered measurements of CM contractility in a clinical context from a scalability perspective. For instance, changes in the peak amplitude and interspike time in response to a drug can be indicative of inotropic and chronotropic effects, respectively. Furthermore, the peak time points in each "active pixel" differed (Figure S1.e) (see details in Figure S1 and experimental: cTFM Data Analysis section). Comparing the peak time point of each pixel with the first emergent peak, the relative time difference can be extracted for each pixel which defines the pixel's latency. (Figure S1.e). Latency in each "active pixel" can be plotted spatially, displaying the lateral timing difference of the hiPSC-CM contraction (Figure 2a,b third panel). The distribution of all latency values in one image of the contracting hiPSC-CMs can be displayed in a line plot, reflecting the percentage probability of a specific latency value (Figure 2d). This distribution can then be compared between samples and considered as a quantitative representation of the delay in mechanical communication of hiPSC-CMs (Figure 2d).

Following the development of our xy-inspection, we shifted to verify the integrity of the hiPSC-CMs bilayer construct, which is particularly vital when considering the analysis of diseased hiPSC-CMs models.[59] In the initial stages of our study, we validated the electrical circuit integrity of the CM layer, ensuring that the cell model of our study is functionally correct.[59] We investigated the electrical activity of hiPSC-CMs with two assays: electrical excitability upon electrical stimulation by xy-inspection and calcium inflow by calcium imaging (see details in Figure S3). Upon electrical stimulation, the hiPSC-CM layer responded practically instantaneously to voltage pulses up to 2 Hz resetting immediately back to spontaneous contraction (Figure S3.a, third panel) upon stopping the pulses. Calcium imaging of the bilayer hiPSC-CMs showed a rapid increase in intensity simultaneously in the whole construct, indicating well-connected cells in the bilayer (Figure S3.c,d). This fast electro-mechanical feedback suggests a complete electrical interconnectivity and functional coupling between the cells.

With the optimized in vitro bilayer model and calibrated xy-inspection, we quantitatively analyzed the contraction of the hiPSC-CM layer, first focusing on the spatial information in the strain/force map. Deformed regions (highlighted colors in Figure 2a,b second panel) were identified on the map. These regions detected from the cTFM measured in the QD channel (Figure 2a second panel) did not spread over the entire image, although the hiPSC-CMs were present in the entire field of view. This indicates that the contraction of hiPSC-CMs detected by the QD is limited on the basal side to areas where the actin-myosin network is connected to the substrate by adhesion. Our observation circles back to the fact that traction in single cells develops mainly at the cell border, corresponding to the adhesion points with the substrate.[21] OPT_BF displayed a contractile region different from that of cTFM (Figure 2b second panel). The observed difference can be attributed to the different inputs since OPT_BF analyzes the BF channel where hiPSC-CMs are moving in all three directions while cTFM detects *x,y* contraction in areas where hiPSC-CMs adhere tightly to the elastomer substrate. The higher spread latency values in the OPT_BF measurement are therefore a potential consequence of the more diverse detected cell layer movements in the *z*-axis compared to the basal contraction, whose traction is limited to the *x*- and *y*-axis. The detected disparity in contraction between hiPSC-CMs on the basal side (cTFM) and those observed in BF (features moving in *x,y*, and *z* axis) (Figure 2a,b second panel) highlights the complex contraction behavior of hiPSC-CM within a layer.

Although different features were tracked, it can be observed that the mean force profiles of the OPT_BF and cTFM samples were similar (Figure 2c). The spatial differences were more prevalent in the timing of the hiPSC-CM contraction, as indicated by the different latency distribution between the two methods (Figure 2d). Addressing the spatial difference shown

https://doi.org/10.1021/acsnano.4c03896
ACS Nano XXXX, XXX, XXX−XXX

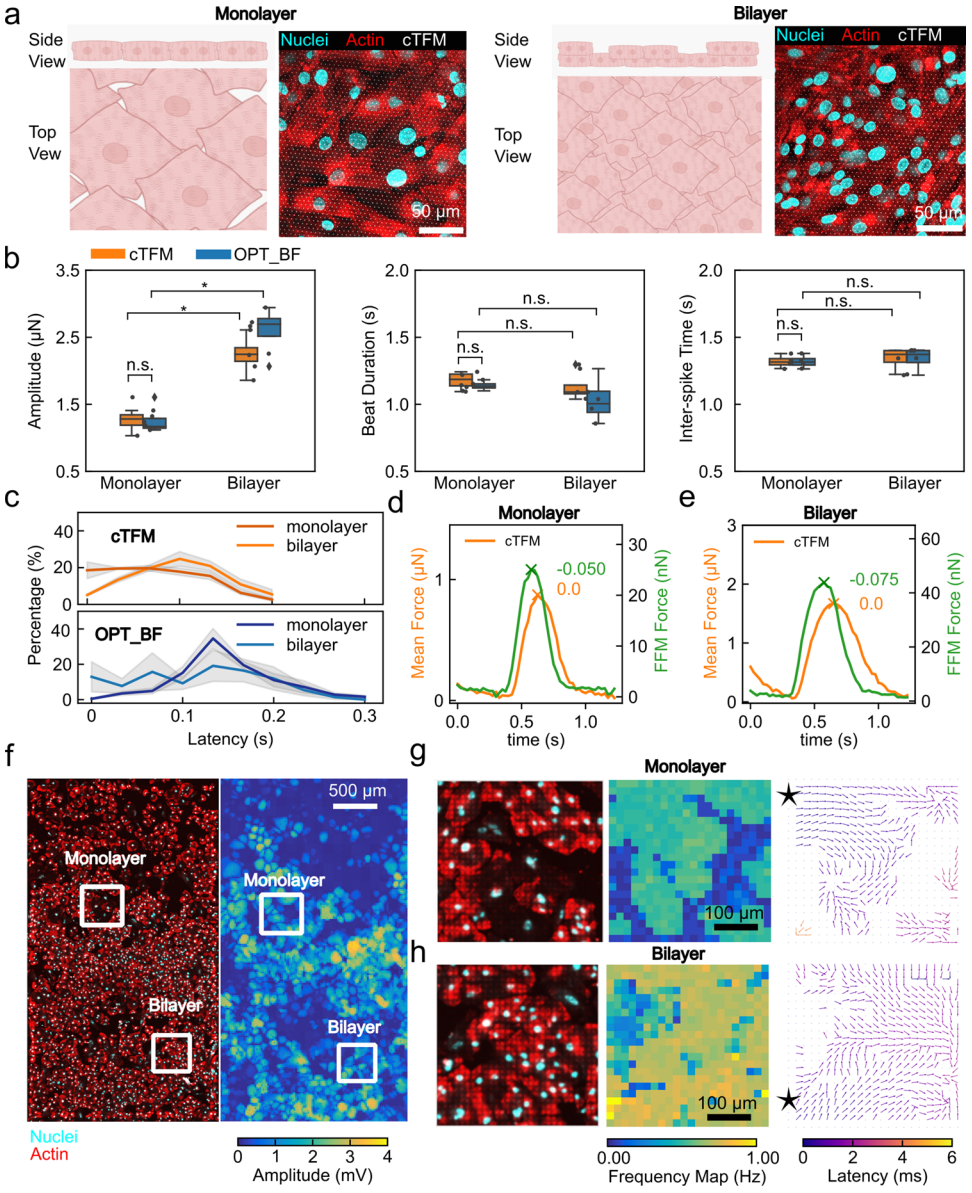

Figure 3. Quantification of mono- and bilayer hiPSC-CMs contraction. (a) Schematic display of the morphological differences in a monolayer (first panel) and a bilayer (second panel) of hiPSC-CM together with examples of immunofluorescent images. (b) Statistical comparison in the amplitude (first panel), beat duration (second panel), and interspike times (third panel) between the two configurations of hiPSC-CMs layer. (c) Corresponding average latency distributions of cTFM (orange: bilayer; darker orange: monolayer) (first row) and OPT (blue: bilayer; darker blue: monolayer) (second row) (N = 4 for both mono- and bilayer hiPSC-CMs). The center line represents the mean and the gray zone covers one time the standard deviation from the mean. Mechanical forces in xy (cTFM: orange) and of z (FFM:green) are recorded simultaneously and are overlaid with highlighted peaks (cross in respective color) for monolayer (d) and bilayer (e) configuration. Corresponding time points of these peaks are shown in text right next to them. (f) Immunostaining of the hiPSC-CMs after recording, cyan indicates nuclei and red indicates α-actin positive cells (first panel). Amplitude of ecAP mapped for the whole HD-MEA chip (second panel). (g) Zoom-in ecAP recordings from the HD-MEA were used to derive the electrical characteristics of monolayer (first row) and bilayer (second row) configuration marked with rectangles in (f), their immunostaining images are in the first panel, and their ecAP frequencies are mapped on the recorded electrode (second panel). Corresponding peak time points of ecAP in active electrodes in the second panel are vectorized in the electrical latency map (third panel) with a black star indicating the starting position of ecAP.

in the map, we further tested the correlation between the OPT_BF applied on this data set and cTFM (details in Figure S4). OPT_BF and cTFM also gave similar values for the timing (Figure S4.b) as well as the amplitude and beat duration (Figure S4.d,e). Moving on to quantitative values, we compared the extracted key parameters (Figure S1.d) across independent samples (N = 4, see experimental: statistical analysis section). Despite the spatial difference in the amplitude map, the mean peak amplitudes showed similar forces between the ±2 and ±2 μN values of OPT_BF (2.6 ± 0.36 μN) and cTFM (2.2 ± 0.31 μN), corresponding to 0.065 ± 0.09 and 0.055 ± 0.08 mN/mm^2 respectively (Figure 2e). This force is similar to the forces obtained by Tulloch et al. using engineered 3D hiPSC-CMs with a mixture of cell types, having contractility of 0.08 mN/mm^2.[60] Averaging latency across samples (N = 4, see experimental: statistical analysis section sec4.9), cTFM and OPT_BF converged at the same latency mean (cTFM: 0.10 s ± 0.008, and OPT_BF: 0.10 ±

https://doi.org/10.1021/acsnano.4c03896
ACS Nano XXXX, XXX, XXX−XXX

0.022 s). However, OPT_BF has a broader latency distribution with a higher full width at half-maximum (cTFM: 0.10 ± 0.049 s; OPT_BF: 0.20 ± 0.062 s). (Figure 2f) This suggests a temporal disparity in contraction between hiPSC-CMs on the basal side and the features across the *z*-axis observed in BF. Combined with the spatial disparity described above, we hypothesize that OPT_BF detects (1) feature displacement on the top layer independently from (2) basal adhesion.

Contraction of hiPSC-CM Mono- and Bilayers. We have demonstrated that our *xy*-inspection is capable of resolving not only the hiPSC-CM contractility but also the mechanical cell−cell coupling through latency analysis. Intuitively, the latency is intricately associated with the number of cell junctions and the cell-ECM interactions. The fact that hiPSC-CM is organized in layers mimics the physiological state with rhythmic contraction and abundant cell−cell connections. To further extend the latency analysis toward quantifying cell−cell interactions, we compared the hiPSC-CM bilayer with a single layer of hiPSC-CMs obtained using reduced seeding densities (confluent monolayer: 1000 cells/mm^2 and confluent bilayer: 2000 cells/mm^2) (Figure 3a).

Structurally, the hiPSC-CM monolayer exhibited slight nuclei enlargement (162.86 ± 50.53 μm^2), with approximately 30 cells occupying an area of 0.04 mm^2 (Figure 3 in the first panel). Conversely, in the bilayer configuration, hiPSC-CMs displayed smaller nuclei (146.35 ± 51.40 μm^2) and a distinctive bilayer structure was observed through a different nuclei location pattern at different z focus in the z stack imaging (Figure 3a second panel, Figure S3.e,f). This manifested as thicker layers with varying levels of homogeneity (Figure 3a second panel side view; Figure S3.e,f). In this configuration, there were approximately 80 cells within the same 0.04 mm^2 area. Contractility quantification of these two configurations revealed a higher peak amplitude of the hiPSC-CM bilayer (≃2.5 μN) than the monolayer (≃1 μN) with a comparable beat duration and frequency (Figure 3b). Apart from the contractility difference, interestingly, a prominent peak around 0.15 s in the latency of the OPT_BF was evident in the monolayer hiPSC-CMs, compared to a flat latency distribution across different values in the bilayer configuration (Figure 3c second row). These two configurations likely involve different timings for contraction, further emphasizing the complexity of evaluating the collective contraction of hiPSC-CMs. Statistically, the monolayer of hiPSC-CMs showed a less delayed mean latency of 0.07 ± 0.011 s and a broader fwhm of 0.133 s, compared to the 0.10 ± 0.008 s average latency and 0.1 s fwhm obtained by cTFM for the bilayer (Figure 3c, first row). We found a similar trend in the OPT_BF measurements (latency mean of bilayer; fwhm of averaged distribution: 0.10 ± 0.022 s; 0.2 s, monolayer: 0.11 ± 0.010 s; 0.033 s) (Figure 3c second row). The broader distribution in the bilayer hiPSC-CM could be due to more diverse moving features in the bilayer hiPSC-CM, including both hiPSC-CMs adhering tightly to the substrate and hiPSC-CMs connecting to each other. Therefore, we could describe the bilayer contraction as more "free-standing" in comparison with the monolayer.

To further investigate the differences between the mono- and bilayer configurations, we conducted a 3D force recording (xyz-inspection).[61] This 3D contractility measurement provided additional information along the *z*-axis, probing on the apical side of the hiPSC-CM layer. Mechanical forces were concurrently recorded in both the *xy*-plane (using cTFM) and the *z* direction (utilizing FFM) (Figures 3d,e and S5; see details in experimental: xyz-Inspection section). The vertical contractility of a hiPSC-CM layer differed spatially in amplitude (Figure S5.b−d),[62] yet preserved the same force profile characteristics such as duration and frequency (Figures 3e, and S5.d). This combined measurement, including the force recorded from FFM at the apical side and from cTFM at the basal side, highlighted the 3D latency. Fixing the cTFM as the reference measurement for the basal side of the hiPSC-CM layer at time t = 0, it appeared that the contractions recorded from FFM occurred earlier in time. Furthermore, the FFM vertical delay (vs cTFM) was larger in the bilayer morphology (0.075 ± 0.014 s), compared to the monolayer (0.050 ± 0.019 s) (Figure 3d,e). This could further confirm the "free-standing" feature of the bilayer configuration, as it contracts with more delay in the *z*-axis.

As electrical signals mark the start of a hiPSC-CM contraction, electrophysiology measurements could investigate further the latency difference between the two configurations.[63] We employed high-density multielectrode arrays (HD-MEA, see experimental: HD-MEA Data Analysis section for further details) to record the extracellular action potential (ecAP) of hiPSC-CMs adherent to the sensor area. The ecAP derived from this methodology was previously validated as a practical indication of the model assay for drug development.[64] Unlike traditional MEA measurements, where recordings include collective ecAP from multiple cells on the same electrode, the HD-MEA measured both the amplitude and the frequency of ecAPs with high temporal and lateral resolution (0.05 ms; 17.5 μm electrode pitch), sufficient to resolve single cell electrical activity and cell−cell electrical communication.[33,34,65] However, HD-MEA sensors are rigid which may stress hiPSC-CMs due to the stiff ECM.[66] This unmatched ECM stiffness in the electrical recording (HD-MEA: GPa) with that of the mechanical measurements (xy- and xyz-inspection: 13.7 kPa[67]) affects the hiPSC-CM contraction characteristic by cell-ECM interaction. Therefore, targeted HD-MEA experiments were performed only to provide additional information with a limited number of independent samples (see details in the experimental HD-MEA Data Analysis section).

Focusing on the cell−cell communication, the lateral morphological characteristics were verified by postexperiment immunofluorescent staining on formaldehyde-fixed samples (Figure 3f first panel), since the HD-MEA are not transparent for microscopy techniques. The amplitude and frequency map of the ecAP corresponded well to the cell coverage (Figure 3f, second panel), matching the fluorescent image (Figure 3f, first panel). In order to measure in detail the electrical activity at the cell−cell interface, zoom-in recordings of the hiPSC-CM were conducted on HD-MEA chips as the maximum number of parallel recording electrodes on the HD-MEA is 1024 (Figure 3g, h). When selecting the recording electrodes, it was possible to identify if the selected cells are in a monolayer or a bilayer configuration comparable to what was defined in the mechanical measurements of the hiPSC-CMs, based on the ecAP activity in the frequency maps and the fluorescent images (Figure 3g,h).

Additionally, corresponding examples of ecAP profiles were averaged for each contraction in these zoom-in recording in Figure S6.a,b. Similarly to the mechanical map, the difference in ecAP peak time points can be extrapolated onto the electrical latency map (zoom-in: Figure 3g,h third panel, whole

https://doi.org/10.1021/acsnano.4c03896
ACS Nano XXXX, XXX, XXX−XXX

chip: Figure S6.c; see details in the Experimental: HD-MEA Data Analysis section). The first emergence of ecAP in all recorded electrodes can be determined due to the high temporal resolution of the MEA system (0.05 ms). Therefore, we mapped the electrical latency with arrows indicating the direction of ecAP propagation based on the latency of ecAP peak timing (Figure 3g,h third panel). Such signal propagation repeated periodically along with the rhythmic contraction of the CMs; therefore, we further extracted the electrical latency distribution to quantify the electrical propagation of the hiPSC-CMs (Figure S6.d,e). The electrical latency map combined with its distribution in a whole chip (most active 1024 electrodes selected) revealed that the ecAP propagated from the left of the chip to the right within 5 ms (Figure S6.c,d, Video S2). Comparing zoom-in recordings of hiPSC-CM in different configurations, the hiPSC-CM monolayer presented a dominant 1.2 ms peak in electrical latency, accompanied by another two peaks at around 2.7 and 4.2 ms (Figure S6.e). These two secondary electrical latency peaks could be due to the hiPSC-CMs at the corresponding positions not being electrically connected to the main hiPSC-CMs electrical event (1.2 ms), as suggested by the latency map.

In contrast, the hiPSC-CMs in a bilayer configuration in which the cells cover the entire field of recording had two main electrical latency peaks at 1.3 and 1.7 ms (Figure S6.e), without other latency peaks at higher values. Although we did not observe a broader latency distribution electrically in the bilayer configuration as in the mechanical measurement, the ecAP propagation differed between monolayer and bilayers, showing a reduction of electrical connection in the monolayer configuration.

The mechanical map of the hiPSC-CM contraction is rich in lateral resolution, providing 0.4 μm/pixel (xy-inspection, xyz-inspection: 0.1 μm/pixel) resolution, showing hundreds of ms mechanical latency difference between layers of hiPSC-CMs. Although the temporal resolution of the mechanical quantification is limited by the inherent acquisition rate of the camera mounted on the microscope (xy-inspection: 0.033 s/frame and xyz-inspection: 0.025 s/frame; field of view: $\simeq$0.04 mm^2), the latency results reported here lay within the range with respect to the long mechanical beat duration (1.2 s) (36 and 48 frames within one contraction for xy-inspection and xyz-inspection, respectively).

The electrical communication of hiPSC-CMs with relatively short ecAPs (duration: 200 ms)[68] can only be resolved with techniques with both high temporal and lateral resolution such as the HD-MEA that is used in this work (Figure 3f–h). Compared to patch clamp, which only allows parallel measurements of a limited number of cells, HD-MEA, which records 1024 pixels with a spatial resolution of 17.5 μm per pixel, provides an improved advantage in resolving cell–cell communication. Moreover, compared with the mechanical latency map, we could derive the electrical propagation path across the cell–cell interface thanks to the high temporal resolution (4000 frames, 50 μs per frame, within one contraction). Therefore, ecAP recording has the suitable spatiotemporal resolution for the hiPSC-CMs electrical communication, described as electrical latency in this work.

Upon comparison of the mechanical and electrical latency, an order of difference in latency values in the mechanical (hundreds of milliseconds) and electrical measurements (ms) was observed. There is indeed an expected time difference between the peak of ecAP and mechanical contraction,[69] which should be in the range of tens of ms due to the cardiac excitation-contraction coupling.[5] However, since each cell (from the one that starts contraction to the one that contracts last) is expected to have about the same inherent time difference, the overall mechanical latency should be the same as the electrical latency. Therefore, the long mechanical latency that we observed here suggests an electromechanical delay as previously demonstrated[70] in a paced hiPSC-CM layer on a rigid substrate, measuring around 100 ms delay of a layer of hiPSC-CMs. We further hypothesized that this delay is also a result of mechanical inertia within the coordinated hiPSC-CM layer, which does not exist in a single hiPSC-CM. Starting from a local action potential, the corresponding hiPSC-CMs initiate their mechanical contraction, which simultaneously exerts pulling on the neighboring hiPSC-CMs. This process repeats in a chain of reactions within a network of hiPSC-CM until the hiPSC-CM layer completes a coordinated beat, which is registered either with cTFM through focal adhesion sites or with OPT_BF through the feature movement. From the macro perspective, the elasticity and local mass of the layer delay the force development in muscle tissue[71] and correlate with the mechanical inertia. The ecAP measured in this work with even shorter electrical characteristics can only enhance this difference in latency. In this work, the degree of mechanical inertia depends on the complexity of interactions such as excitation-contraction coupling within each cell, cell–cell connections, and cell-ECM interactions. Compared to a previous electromechanical wave study by Liu et al. (30 μm),[70] we presented a higher lateral resolution with contractility quantification, resolving the mechanical coupling of hiPSC-CM with each other, which is especially complicated in the hiPSC-CM layer.

The broad latency distribution of hiPSC-CM contraction observed from both mechanical and electrical measurements could arise from the inherent limitations of hiPSC-CMs in establishing connections with each other.[72] The mechanical inertia in hiPSC-CMs can be explored more thoroughly via an in vitro model that includes supporting cells, such as cardiac fibroblasts which could modulate the mechanical coupling by producing ECM.[72] The physical linkage between the ECM and the cytoskeleton, established by the focal adhesions, controls the complex bidirectional mechanical forces. Previous studies have shown that substrate stiffness influences the expression of the connexin isoform 43 and the calcium handling of hiPSC-CMs[49] as well as their contractility.[73] CMs on stiffer substrates have a larger contractility in xy[73] and a smaller force in z[49] compared to CMs on soft substrates, suggesting that when contracting, CMs deform easier in 3D when adherent on softer substrates.[74] In the bilayer configuration, the top layer binds to the bottom hiPSC-CMs which has a Young's modulus of 1.25 kPa,[75] while the bottom layer adheres to the cTFM substrate or the HD-MEA, which has a modulus of 13.7 kPa or tens of GPa, respectively. From the mechanotransduction perspective, it is not surprising to observe the different mechanical and electrical propagation patterns between the bilayer and the monolayer of hiPSC-CMs. Moreover, mechanical conduction is faster with CMs adherent to a softer substrate.[49] This matches the observations of mechanical latency differences found between the hiPSC-CM bilayer and monolayer with xy-inspections, where more diverse latency values were present in the hiPSC-CM bilayer configuration. Therefore, we attribute the larger mechanical inertia, indicated by the decreased mean latency detected by cTFM and the broader latency distribution

https://doi.org/10.1021/acsnano.4c03896
ACS Nano XXXX, XXX, XXX–XXX

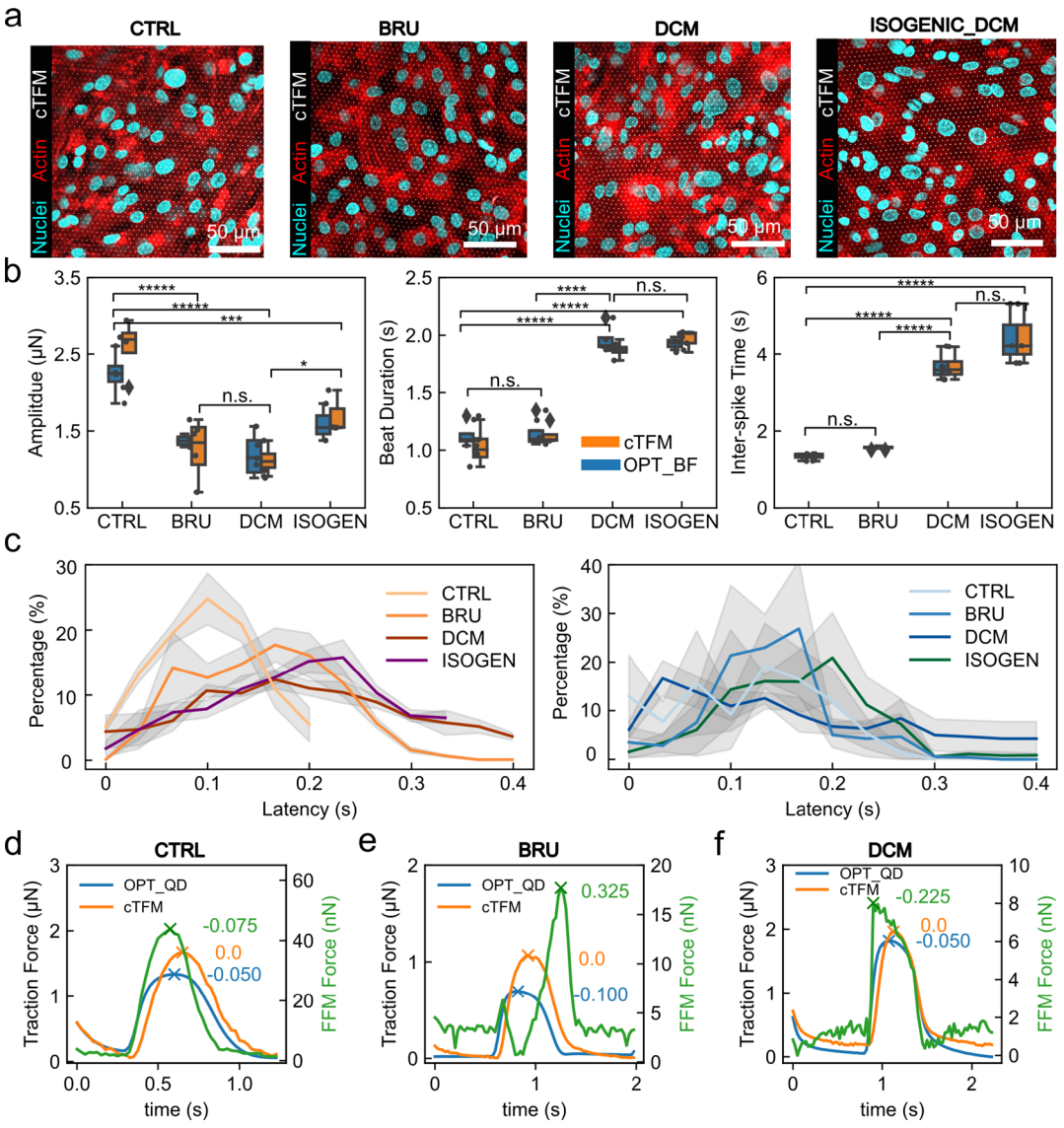

Figure 4. Quantification of diseased hiPSC-CMs contraction. (a) Immunofluorescent staining of CTRL, BRU, DCM, and isogenic DCM diseased cell lines in a bilayer configuration. (b) Contractility quantification of hiPSC-CMs analyzed by xy-inspection providing statistical comparison in amplitude (first panel), beat duration (second panel) and interspike time (third panel) ($N = 4$ for all conditions, n.s. stands for not significant, * $p < 0.05$, ** $p < 0.001$,* $p < 0.0001$,**** $p < 0.00001$,***** $p < 0.000001$). (c) Latency distributions of CTRL, BRU, DCM, and ISOGEN analyzed by cTFM (first panel) and by OPT_BF (second panel). Xyz-inspections on CTRL (d), BRU (e), and DCM (f), providing 3D force profiles with peak time points indicated next to the peaks.**

seen in OPT_BF (Figure 3c), to the "free-standing" characteristics of the hiPSC-CMs bilayer. Furthermore, more feature movements covering the hiPSC-CM contraction in the vertical axis in the bilayer configuration were measured by a larger 3D latency delay than the monolayer configuration with xyz-inspection. A further detailed investigation into the coupled cell-ECM and cell−cell interactions could include a soft ECM surrounding CMs, such as a hydrogel-based cell encapsulation system while recording the local contraction with high lateral resolution.

Contraction of Diseased hiPSC-CMs. The coordination of the hiPSC-CMs in a layer does not only rely on the cooperative coupling of the cell-ECM and cell−cell interactions but is also tightly correlated to the functional contraction of every single hiPSC-CM, all of which can be altered by diseases and pathological conditions. After characterizing the contraction of hiPSC-CMs from healthy donors both electrically and mechanically (CTRL), we extended the study with two different diseased hiPSC-CM cell lines (Brugada syndrome and Dilated Cardiomyopathy) to assess whether these diseases modify any of the previously described quantitative parameters (Figure 4).[7,10] f4

Brugada syndrome is a hereditary ion channel disorder that increases the risk of ventricular arrhythmias and sudden cardiac death. Here, we used engineered hiPSC-CMs with artificially introduced Cav1.2 (CACNA1C: loss-of-function) gene (G490R specifically) into a donor with no known disease-related genotypes (BRU) (Figure 4 is a second panel). Cav1.2, a voltage-gated L-type calcium channel, serves as a crucial mediator of the cardiac action potential.[76] Given its function as the primary channel regulating calcium entry for excitation-contraction coupling, the loss of function in this channel leads to bradycardia and arrhythmias.[76] Dilated cardiomyopathy (DCM) is typically diagnosed clinically by ventricular dilation

https://doi.org/10.1021/acsnano.4c03896
ACS Nano XXXX, XXX, XXX−XXX

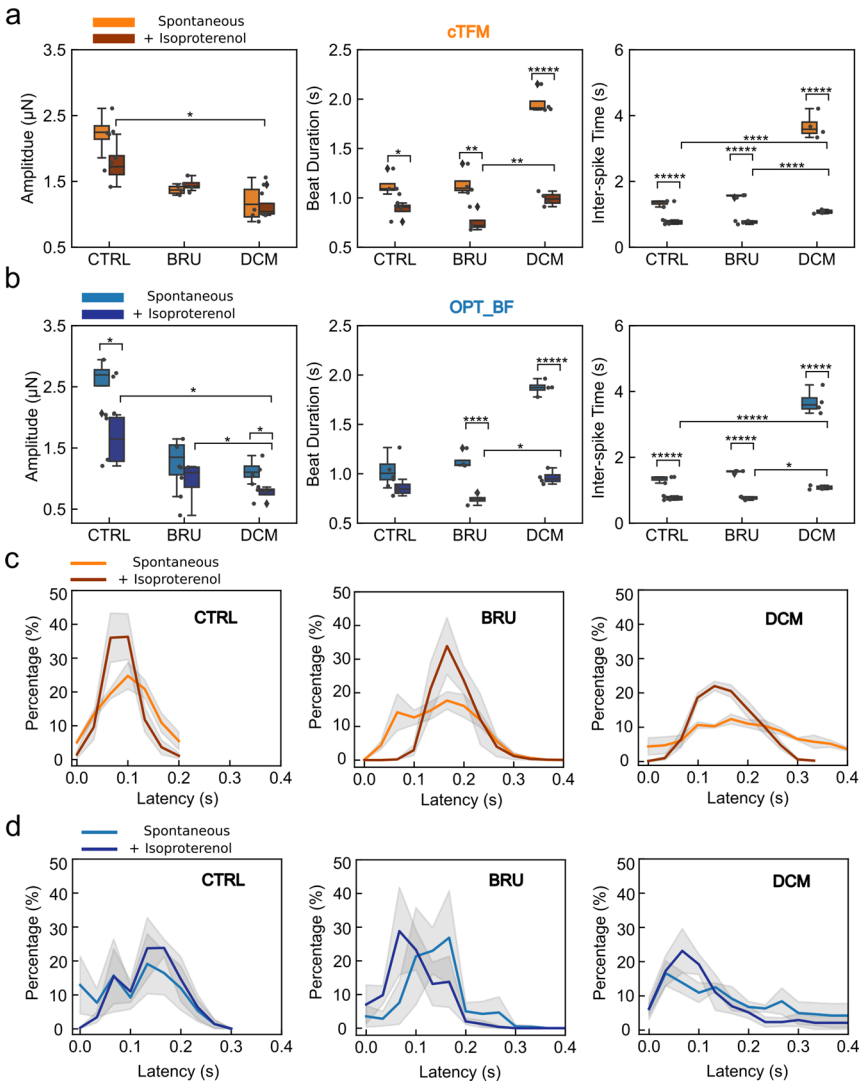

Figure 5. Response of hiPSC-CMs to isoproterenol. Contraction quantification and latency distributions with (a, b) cTFM and with (c, d) OPT_BF of spontaneously beating and isoproterenol stimulated hiPSC-CMs in CTRL, BRU, and DCM conditions. CTRL (N = 4), BRU (N = 4), and DCM (N = 4) (* p < 0.05, ** p < 0.001, *** p < 0.0001, **** p < 0.00001, ***** p < 0.00001. Not labeled statistics are not significantly different.

and reduced heart contractility, representing a disease in which mechanobiology plays an important role.[10] In our study, we focused on hiPSC-CMs derived from an individual with DCM pathology, specifically a donor carrying lamin A/C (LMNA: L35P) protein mutation[10] (DCM) (Figure 4a third panel). To expand the application of our methodology in the genetic etiology of DCM, we introduced the engineered isogenic control of DCM with L35P correction, as stated by the producer (ISOGEN) (Figure 4a fourth panel).

We have quantitatively assessed the behavior of both mono- and bilayers of the diseased hiPSC-CMs by using the methodology described above. Monolayers hiPSC-CMs mainly differed in interspike time (Figure S7.c), especially between CTRL and BRU. Bilayers hiPSC-CMs seemed to have a more pronounced difference in the measured overall mechanical quantitative parameters (Figure 4). Consequently, we chose to focus on the hiPSC-CM bilayer condition for both healthy and diseased cell lines, as it is also more relevant for the study of cell−cell interactions.[3] Statistical results revealed that both BRU and DCM have a reduced beating amplitude, with both cTFM and OPT_BF being in agreement (Figure 4b). DCM had a longer beat duration and interspike time (lower beating frequency) than BRU and CTRL and sometimes showed arrhythmia detection which indicates a more severe mechanical pathological condition, matching the reduced contractility of DCM samples (Figure 4b). The ISOGEN displayed an increased trend in amplitude compared to DCM hiPSC-CMs, however still had a longer beat duration and higher interspike time compared to the healthy hiPSC-CMs (Figure 4b). Such observation indicates that the DCM pathology involves additional genetic mutations other than the L35P, resulting in a reduced contraction.[58] The comparison of the isogenic control of DCM alleviates the differences in the genetic background of the donor of hiPSC-CMs, focusing the quantification on the specific genetic mutation. This further highlights the significance of hiPSC-CMs in the study.

After a statistical analysis of the diseased hiPSC-CMs, we focused on latency comparison. cTFM measured increasingly higher fwhm of latency distributions for BRU (0.17 s) and DCM (0.20) compared to CTRL (0.10 s). The mean latency of DCM and BRU measured from cTFM shifted toward higher values (BRU and DCM averaged at 0.16 ± 0.016 and 0.20 ±

https://doi.org/10.1021/acsnano.4c03896
ACS Nano XXXX, XXX, XXX−XXX

0.029 s respectively vs CTRL at 0.11 ± 0.010 s) (Figure 4c first panel).

OPT_BF analysis had less obvious trends in latency distribution but also displayed a greater percentage of higher latency values measured in BRU and DCM (Figure 4c second panel). The delay in latency means detected by OPT_BF became more severe with DCM, having an average of 0.21 ± 0.033 s (CTRL: 0.10 ± 0.022 s). This difference was less pronounced in BRU samples measured by OPT_BF, with an average latency of 0.16 ± 0.024 s (Figure 4c, second panel).

The xyz-inspections of the diseased hiPSC-CMs revealed distinct characteristics compared to healthy hiPSC-CMs (Figure 4c–e). In BRU samples, a notable double-peak feature and an FFM latency of 0.325 ± 0.224 s compared with the cTFM measurement in the contraction was observed (Figure 4d). Likewise, in DCM, a large 3D latency difference was seen, with −0.225 ± 0.122 s in the FFM anticipated to the cTFM (Figure 4e). These 3D latency features of BRU and DCM suggested irregularities in mechanical conduction along the *z*-axis in diseased hiPSC-CMs.

Apart from the measured contractility reduction, also a noticeable delay in mechanical latency was observed in the diseased hiPSC-CM layer, suggesting a larger mechanical inertia. This could stem from the defective coupling between hiPSC-CM within the layer. Specifically, DCM hiPSC-CMs have the LMNA defect, which results in reduced force transmission from the sarcomere to the ECM, leading to the broadest latency distribution. At the same time, the defective mechanical coupling in BRU is interesting as the Cav1.2 defect is not typically associated with mechanical disorders. The fact that an ion channel defect results in larger mechanical inertia indicates the important role of excitation-contraction in the mechanical coupling of hiPSC-CMs.

The characterization of the electrical activity of diseased cell lines is equally essential in identifying pathological conditions.[8,13] The loss-of-function Cav1.2 in BRU samples generates a shortened action potential duration and short QT intervals with a reduced calcium current.[7] Therefore, we expected to find the observed differences in the electrophysiological behavior of the BRU hiPSC-CMs. Similarly, although DCM primarily affects the heart structure mainly by ventricular dilation, it also leads to electrical abnormalities as a secondary consequence.[8] Despite the rigidity mismatch between mechanical and electrical measurements, HD-MEA was needed for electrical characteristic registration of diseased hiPSC-CMs (details in Figure S8). The latency analysis showed that ecAP propagation in BRU has a higher delay compared to that in the healthy hiPSC-CMs (Figure S8). This electrical delay may be attributed to the loss of function in calcium channels, leading to an overall reduced Ca^{2+} trafficking in each hiPSC-CM and also between hiPSC-CMs. DCM hiPSC-CMs by definition are "mechanically defective"[9] and our analysis demonstrated a milder delay with a latency; the correction of the LMNA mutation (Isogenic DCM) leads to a recovery of the electrical propagation (see details in Figure S8). The limitation of this study is the separate recording of the electrical and mechanical activity, performed on different platforms with drastically different rigidity. An envisioned improvement would be the simultaneous mapping of the electrical and mechanical activities to further investigate the effect of cell–cell and cell-ECM coupling by using, e.g. different seeding densities and tunable substrate Young's modulus.

Response of hiPSC-CM Bilayers to Isoproterenol. Finally, we investigated how the in vitro models (CTRL, BRU, and DCM samples) respond to isoproterenol to assess the suitability of our platform for investigating drug-induced effects. We treated the hiPSC-CMs with isoproterenol (1 μM), which is known to upregulate the cardiac β-adrenergic pathway with an expected increase of contractility, beating frequency (positive inotropic and chronotropic effects), and conduction velocity.[77−79] Overall, we did not measure any positive inotropic effect of isoproterenol (Figure 5a first panel), which can be an indication of the immaturity of the hiPSC-CMs, as reported in the literature.[22,80,81] A positive chronotropic effect was confirmed in both cTFM and OPT_BF by the two-fold decrease in the interspike time and a halving of the beating duration compared to the untreated hiPSC-CMs (Figure 5a,b).

Focusing on the response of the diseased hiPSC-CMs toward isoproterenol, BRU hiPSC-CM samples were majorly rescued with shortened beat duration and a smaller interspike time, while DCM hiPSC-CMs still presented significantly longer beats and interspike time compared to the untreated CTRL (Figure 5a,b). We found no significant differences in average latency between spontaneous (cTFM: 0.1 ± 0.008 s; OPT_BF: 0.10 ± 0.022) and isoproterenol treated (cTFM: 0.09 ± 0.006 s; OPT_BF: 0.10 ± 0.016) contraction of CTRL. Similarly for BRU, which showed an average latency at 0.18 ± 0.025 s (OPT_BF: 0.12 ± 0.022 s) with isoproterenol (Figure 5c,d, second panel) compared to 0.16 ± 0.016 s (OPT_BF: 0.15 ± 0.024 s) for spontaneous contraction. In contrast, we observed a larger latency mean change in DCM compared to BRU, exhibiting a smaller mean latency centered at 0.16 ± 0.013 s (OPT_BF: 0.16 ± 0.05 s) compared to spontaneous beating (0.21 ± 0.03 s, OPT_BF: 0.21 ± 0.033 s) (Figure 5c,d, third panel). Importantly, a clear narrower latency distribution in all cell types is measured by cTFM with the fwhm of the mean distribution compared in spontaneous and isoproterenol-treated contraction (CTRL: 0.10; 0.03 s; BRU: 0.17; 0.07 s; DCM: 0.20; 0.10 s) (Figure 5d first panel). The same trend is also observed in the OPT_BF analysis (CTRL: 0.20; 0.13 s, BRU: 0.07; 0.03 s, DCM: 0.23; 0.07 s; Figure 5d, second panel).

To summarize, the latency analysis measures a partial mechanical coupling recovery by isoproterenol, which demonstrates the sensitivity of the mechanical measurements, making it also applicable in drug assessment. The decreased mean latency in DCM samples with isoproterenol confirms what in the literature has been assessed as the role played by impaired Ca^{2+} trafficking, a key dysfunction contributing to arrhythmogenesis in this cardiomyopathy.[82] The unchanged mean latency in BRU indicates that the enhanced calcium trafficking from the β-adrenergic receptor activation could not fully compensate for the defective excitation-contraction coupling caused by the loss of function in the calcium voltage-sensitive channel mutation.[83,84]

The β-adrenergic upregulation observed in the mechanical activity can also be observed in the parallel electrical measurements (details in Figure S9), with targeted experiments on CTRL and BRU, again considering the effect of rigid HD-MEA on cell-ECM interactions. We compared the ecAPs of hiPSC-CMs within the same zoom-in field of view under spontaneous contraction and after isoproterenol stimulation (Figure S9). In healthy hiPSC-CMs, the spontaneous frequency of ecAP doubled (0.5 Hz vs 1 Hz under

https://doi.org/10.1021/acsnano.4c03896
ACS Nano XXXX, XXX, XXX−XXX

isoproterenol treatment), and the latency distribution shifted toward lower values with a peak at 0.78 ms, in contrast to spontaneous activity (1.64 ms) (Figure S9.a–c). The BRU response to isoproterenol was electrically present, not only in the chronotropic effect but also in the altered latency distribution (Figure S9.d–f). In the electrical latency map, we observed a different conductive pathway in the isoproterenol-stimulated BRU, where the ecAP propagates faster from the lower right to the middle until the upper regions of the field of view (Figure S9). This also aligns with the accelerated conduction velocity by β-adrenergic modulation from isoproterenol.[77,79]

CONCLUSIONS

In this work, cTFM and OPT_BF served as mutual validation in quantifying the hiPSC-CM contractility and together demonstrated great potential in measuring the cell–cell mechanical coupling. Specifically, the introduced xy-inspection and xyz-inspection complemented the traditional contraction analysis with latency quantification. Furthermore, the electrical latency was characterized by targeted ecAP mapping with HD-MEA, resolving the electrical propagation pathway within the hiPSC-CM layers. We provided a complete set of latency evaluations, being able to distinguish between mono- and bilayer hiPSC-CM configurations and between healthy and diseased hiPSC-CM layers. Combined with contraction measured with FFM at the z-axis, a more spread latency in a bilayer hiPSC-CM configuration was shown in both 2D and 3D, highlighting the larger mechanical inertia in the bilayer configuration. In diseased hiPSC-CM layers, a noticeable delay in both mechanical and electrical latency was observed, indicating defective coupling between hiPSC-CM within the layer. This defected coupling could be partially rescued with the activation of the β-adrenergic pathway, validating the applicability of the proposed technique for drug assessment. In conclusion, the mechanical and electrical analyses proposed in this work provided different insights into the signal conduction of cardiac in vitro models. Notwithstanding that the hiPSC-CM mono- and bilayers do not have the grade of biological complexity to be rationalized as multilayers or 3D models, they ensure a high sensitivity enough to reliably detect pathological conditions for possible applications in pharmaceutical research.

EXPERIMENTAL SECTION

Fabrication of cTFM Substrates. Glass coverslips were first spin-coated with CY52–276 silicone (DOWSIL, USA) using a 9:10 mixing ratio with components A and B, resulting in an elastic modulus of approximately 13.7 kPa.[45,61] Details of the silicone preparation can be found in the study of Reyes Lua et al.[67] Subsequently, red-emitting quantum dots (CdSe, QD) in the form of nanodiscs were precisely deposited onto these silicone substrates in hexagonal arrays (210 × 210 μm^2 each), maintaining a spacing of 5 μm between discs. This deposition was achieved using the electrohydrodynamic nanodrip printing technique, as previously reported by Bergert et al.[45] For the experiments, the prepared substrates were fixed to bottomless Petri dishes (WillCo Wells, NL) for cell culture with double-sided adhesive provided by the Petri dish manufacturer.

Cell Culture. hiPSC-CMs were purchased from Fujifilm Cellular Dynamics Solutions (USA). The CTRL hiPSC-CM was derived from a healthy donor clone 11,713. BRU hiPSC-CM was an artificial cell line that engineered the Cav1.2 loss-of-function gene in a healthy donor with clone number 01434. DCM hiPSC-CM was derived from individual mice (clone 01016) with dilated cardiomyopathy. Isogenic control of DCM hiPSC-CM was corrected with the L35P genetic missense of the DCM hiPSC-CM cell line. xy-inspection and xyz-inspection use the cTFM substrate prepared with the same methods described above. The cTFM substrates were coated with vitronectin (Sigma, USA) (50 μg/mL in DPBS (Thermo Fisher, USA)) for 2 h at 37 °C before cell seeding, and finally washed with DPBS twice before cell seeding.

Cells were thawed and handled according to the manufacturer's recommendations, in terms of the warm-up procedure and usage of specific medium. Two seeding densities were used to obtain either monolayers (1000 cells/mm^2) or bilayers of cells (2000 cells/mm^2).

The HD-MEAs (Maxwell Biosystems, Switzerland) were prepared with the same coating protocol as the cTFM substrate described before; 100,000 cells were seeded on each HD-MEA. Two days after plating, the plating medium was replaced with a maintenance medium supplied by Fujifilm to guarantee cell viability and functionality. Cells were incubated at 37 °C and 5% CO_2 for at least 10 days to allow for proper cell attachment to the substrate. The maintenance medium was refreshed every 2 days during the whole experiment according to the manufacturer's instructions.

xy-Inspection. Both BF and fluorescent (cTFM: QD) images were acquired by a confocal laser scanning microscope (CLSM) (Olympus Fluoview FV3000) with temperature and CO_2 control. A 488 nm argon laser was band-passed before illuminating the sample and exciting red QDs with an emission window of 550 to 650 nm. One minute acquisition on each sample were acquired with a 60× objective, having a numerical aperture of 1.35, at 30 frames/s.

xyz-Inspection. We selected FluidFM commercial tipless silicon nitride probes (Cytosurge AG, Switzerland) with a 2 μm circular aperture and low spring constants (initially 0.2 N/m). According to the thermal tuning calibration,[85–88] these probes have an average spring constant of 0.26 N/m. The deflection sensitivity was calibrated by averaging the slopes of deflection versus voltage from four forward force spectra recorded on glass in PBS (Thermo Fisher, USA) before each experiment. A 4 μm bead (Degradex, USA) was attached to the cantilever with negative pressure. The experiments were conducted at 37 °C within an incubation chamber (Life Imaging Services, Switzerland). The cTFM samples with a hiPSC-CM layer were mounted on a live-cell, wide-field fluorescent microscope (Axio observer, Zeiss, Germany) equipped with the FluidFM system (FlexAFM-near-infrared scan head with a C3000 controller driven by the EasyScan2 software, Nanosurf AG, Switzerland). The highest point within the hiPSC-CM layer was selected for probing based on a z-stack of images. For each experiment, we selected 2–3 highest points to measure the z force. The approach set-point for force detection was set at 10 nN to ensure a gentle yet effective contact between the cantilever and the hiPSC-CM layer. The imaging of cTFM in the red channel was performed with a CMOS ORCA-flash camera (Hamamatsu, Japan) using a 63× objective, having a numerical aperture of 1.34 at 40 frames/s. The simultaneous recording of imaging information (shutter opening), deflection, and piezo movement was integrated into a DAQmx device (BNC-2090A, National Instruments, US). The force recorded with FluidFM and cTFM can then be synchronized based on the shutter opening, assigning the correct z force to the xy force in time.

Immunostaining. Samples were fixed with 4% formaldehyde solution (Sigma-Aldrich, USA) for 10 min at room temperature. After fixation, the samples were washed three times for 5 min with 1× Phosphate buffer solution (PBS, Gibco, USA). Permeabilization of the cell membranes was performed with a 10 min incubation step in Dulbecco's phosphate buffered solution (DPBS, Gibco, USA) supplemented with 1% bovine serum albumin (Sigma-Aldrich, USA) and 0.1% Triton-X100 (Sigma-Aldrich, USA). After washing thoroughly with 1× DPBS, the samples were incubated with primary antibody (Mouse Antisarcomeric Alpha-actin, Abcam, MS-295, UK) resuspended with a dilution factor of 1:200 in blocking buffer (DPBS with 0.1% goat serum), overnight at 4 °C. On the following day, after washing steps, incubation with the secondary antibody solution diluted in the blocking buffer (Alexa Fluor 488 goat antimouse, concentration 1:100, Thermo Fisher Scientific, A28175, USA) was performed for 2 h at room temperature. Lastly, after the unbound antibody was washed off, the samples were incubated with Hoechst

https://doi.org/10.1021/acsnano.4c03896
ACS Nano XXXX, XXX, XXX–XXX

33342 solution (Thermo Scientific, 62249, USA). Finally, the cells were imaged within 2 days to prevent any bleaching of the immunofluorescent signal.

cTFM Data Analysis. To calculate the traction forces during hiPSC-CM beating, we employed image analysis using the previously developed software, Cellogram,[51] which does not require a reference image. Instead, it relies on establishing the theoretical initial position of the ordered QD nanodisc array and comparing it with the experimentally acquired images to determine the QD displacement field $\mathbf{\Delta u}$. Subsequently, using the known material properties of the substrate, the traction force vector field $\mathbf{F}$ was computed with a linear elastic material model[51]:

$$\mathbf{F} = \frac{E}{2(1+\nu)}\mathbf{\Delta u} + \frac{E}{2(1+\nu)(1-\nu)}\nabla(\nabla\cdot\mathbf{\Delta u}) \quad (1)$$

where E is the elastic modulus of the material (13.7 kPa here), and ν is the Poisson ratio (0.49 for our CY elastomer substrate). Then, the modulus of the projection of the traction force $\mathbf{F}$ onto the xy plane is

$$F_{xy} = \sqrt{F_x^{\,2} + F_y^{\,2}} \quad (2)$$

Traditionally, F_{xy} is expressed in kPa (0.001 N/mm^2) to be subsequently multiplied by the area of each pixel (0.16 μm^2 for xy-inspection images, while 0.01 μm^2 for xyz-inspection images due to the better objective on the xyz-inspection setup).

Additionally, a filter step is incorporated into the analysis to extract the pixels of the actually deformed regions with a mask to subtract the noise. In this step, we utilize both images of the rest of the state and the contracted state of hiPSC-CMs as a reference. A threshold of 0.3 × the standard deviation of the contracted state of hiPSC-CMs was added to the background recorded at the rest of the state of hiPSC-CMs for each pixel. Pixels below this threshold were excluded in the final mask (black pixels in Figure S1.a). The final mask generated was then projected onto the raw traction force map. The corresponding force profile of each pixel in the masked map was preserved for the extraction of peak amplitudes and timing (Figure S1.a).

The mean of these force profiles (pixels within the masked traction force map) was then defined as the force profiles of the hiPSC-CMs within the field of the view, and a peak-detection algorithm (modified based on the find peaks function (scipy, python)) was applied to output the peak time points and contractility indications such as peak amplitude, beat duration, and interpeak time (Figure S1.b). The peak time point of each pixel (within the masked traction force map and within the beat) was extracted (Figure S1.e). Then these time points were subtracted from the earliest peak time point, yielding values that begin with 0 and end with a threshold (0.3 s for healthy hiPSC-CMs, 0.4 s for diseased hiPSC-CMs). These differences are defined in this study as latency values, and the distribution of the latency values can be plotted in a line plot, with latency time as the x-axis and the percentage of each latency value as the y-axis (Figure 2d). The latency of each pixel can be presented on a latency map (Figure 2a,b, third panel). The latency distributions could be further compared and averaged between individual samples, and the center line is the mean over different samples, and the gray zone covers all points within the standard deviation (Figure 2f). The full-width half-maximum (fwhm) of the mean latency distribution over different samples is extracted to describe how spread the distribution is. The latency distribution is referred to in this study as a delay and is used to compare the efficiency of cell−cell mechanical communications between different hiPSC-CMs configurations and cell lines.

OPT_BF Data Analysis. The OPT software was developed in Matlab (Matlab 2023a, The Mathworks Inc., USA) and it was based on movement tracking with automatic feature detection relying on the Kanade-Lucas-Tomasi (KLT) algorithm,[52] which is a recognized approach for feature extraction with the advantage of computational discharge.[53,54] The whole batch of features returned by KLT was processed and filtered. The displacement of the selected features (green crosses in Figure 2b first panel) was calculated in x (dx_i) and y component (dy_i) for each feature i between time points 0 and t. The calibration factor to switch from the image reference system to the actual contraction in physical units (μm) was calculated according to the approach by Sala et al.[42] The traction force in x,y is linearly dependent on the displacement and inversely to the G matrix (eq 3).[55] The traction force was calculated from the Boussinesq equation, under a small displacement assumption.[56]

$$F = G^{-1}\cdot[dx_i,\ dy_i,\ 0] \quad (3)$$

G matrix integrates the displacement with Young's modulus (E) and the Poisson ratio ν of the substrate to which the hiPSC-CMs adhered in the system, as hiPSC-CMs drag the substrate while contracting.[55]

$$G_{\text{matrix}} = \begin{bmatrix} g_{11} & g_{12} & g_{13} \\ g_{21} & g_{22} & g_{23} \\ g_{31} & g_{32} & g_{33} \end{bmatrix} \quad (4)$$

Components within the G matrix are

$$\begin{aligned}
g_{11} &= \frac{1+\nu}{2\pi E}\cdot\left(\frac{2\left(1-\nu\right)\cdot\sqrt{d_x^2+d_y^2}}{d_x^2+d_y^2} + \frac{2\sqrt{d_x^2+d_y^2}\left(\nu\cdot\sqrt{d_x^2+d_y^2}\right)\cdot d_x^2}{\left(d_x^2+d_y^2\right)^3}\right)\\
g_{21} &= \frac{1+\nu}{2\pi E}\cdot\left(\frac{2\nu\cdot\left(d_x^2+d_y^2\right)\cdot d_x d_y}{\left(d_x^2+d_y^2\right)^3}\right)\\
g_{12} &= g_{21}\\
g_{31} &= \frac{1+\nu}{2\pi E}\left(\frac{(1-2\nu)\cdot d_x}{d_x^2+d_y^2}\right)\\
g_{13} &= -g_{31}\\
g_{22} &= \frac{1+\nu}{2\pi E}\cdot\left(\frac{2\left(1-\nu\right)\cdot\sqrt{d_x^2+d_y^2}}{d_x^2+d_y^2} + \frac{2\sqrt{d_x^2+d_y^2}\left(\nu\cdot\sqrt{d_x^2+d_y^2}\right)\cdot d_y^2}{\left(d_x^2+d_y^2\right)^3}\right)\\
g_{32} &= \frac{1+\nu}{2\pi E}\left(\frac{\left(1-2\nu\right)\cdot d_y}{d_x^2+d_y^2}\right)\\
g_{23} &= -g_{32}\\
g_{33} &= \frac{1+\nu}{2\pi E}\cdot\frac{2(1-\nu)}{\sqrt{d_x^2+d_y^2}}
\end{aligned} \quad (5)$$

Detected features within the traction force map underwent the same peak detection algorithm and the extraction of the peak time points, which was used later to output latency values. They can be further visualized in the latency map and latency distribution as cTFM.

HD-MEA Data Analysis. In both whole-chip and zoom-in recordings of the hiPSC-CMs, the ecAP at each electrode was acquired and analyzed. From the profile of each ecAP, which is the ecAP plotted over time, the maximum absolute amplitude, the frequency of ecAP, and the time point of the absolute maximum amplitude (time stamp of this ecAP) were extracted (Figure S6.f, dashed lines). The maximum amplitude and the frequency of ecAP were plotted at each electrode location, generating the spatial amplitude and frequency maps (Figure 3f−h). The whole chip amplitude maps of the hiPSC-CMs on the HD-MEA were generated by subsequently routing 25 different electrode configurations,

https://doi.org/10.1021/acsnano.4c03896
ACS Nano XXXX, XXX, XXX−XXX

recording for 30 s for each configuration, and then stitching all results together. The latency maps were derived from the time stamps of ecAP recorded on each electrode. The first occurrence of a spike event (the first time stamp) within a contraction (all electrodes averaged in the field of view) can be found thanks to the high temporal resolution of the recording system (50 μs). Assigning this earliest spike event as time 0, the relative latency time on other active electrodes can be mapped (Figure 3g,h third panel) This approach yields latency maps with vectors indicating the direction of the ecAP flow. This process of analyzing time stamps and assigning them spatially was based on a previously developed software package: *Neuroflow*.[65,89] Subsequently, these latency values recorded at all electrodes can be extracted, and their probability can be visualized as a latency distribution (Figure S6.d,e). We performed two whole-chip recordings for CTRL and BRU hiPSC-CMs, and one whole-chip recording for DCM, ISOGEN. Within the whole chip recordings of CTRL and BRU, at least 5 zoomed-in recordings were acquired.

Statistical Analysis for the xy-Inspection. One recording (at least 1 min recording) from one sample seeded at a certain date was considered as an "independent" sample, on which several (from 10 to 20) 200 × 200 μm^2 regions were imaged contributing to the mean values for that sample. The number of biologically independent experiments, i.e. of samples seeded at different substrates and at different dates, was indicated as *N* in the caption or the text of each figure. The number of independent experiments analyzed for each condition were as follows: CTRL bilayer: 4, CTRL monolayer: 4, BRU monolayer: 4, BRU bilayer: 4, DCM monolayer: 4, DCM bilayer: 4, and Isogenic DCM bilayer: 3. Each sample had a paired spontaneous and isoproterenol-stimulated result. These numbers are also reported in the figure captions. The statistical tests were performed using a home-built Python script. The Shapiro-Wilk test was used to evaluate the normality of the data. For normally distributed data, the *t-test* was performed. For data with several groups (diseased states), the one-way ANOVA with pairwise Tukey multiple comparisons test was performed. For all tests, a specificity of 0.05 was set. In all box plots, the population median was indicated as a horizontal line inside the boxplot. The box covers the first quartile to the third quartile of the data. The whiskers extend from the box to the farthest data point lying within 1.5× the interquartile range from the box. Scattered dots are each experimental data point, outliers are marked as diamonds (n.s. stands for not significant, * $p < 0.05$, ** $p < 0.001$, *** $p < 0.0001$, **** $p < 0.00001$, ***** $p < 0.00001$).

The latency distributions were averaged over independent samples and were plotted as latency time versus probability as a percentage of that latency. The standard deviation above and below the mean was indicated with a gray zone.

ASSOCIATED CONTENT

Data Availability Statement

X.Z. and M.B. contributed equally to this work.

Supporting Information

The Supporting Information is available free of charge at https://pubs.acs.org/doi/10.1021/acsnano.4c03896.

Raw data (hiPSC-CM beating -treated with isoproterenol- in both QDs and BF channel) and processed data (inferred by both cTFM -force video and latency map- and OPT_BF images) (MP4)

Processed data, ecAP propagation of a hiPSC-CM bilayer on a HD-MEA (MP4)

Figure S1: derivation of force maps from cTFM images during hiPSC-CM contraction; Figure S2: OPT stability against various brightness; Figure S3: electrical excitability and connectivity of hiPSC-CM bilayers; Figure S4: force profile characteristics and correlation between cTFM and OPT_BF; Figure S5: xyz-inspection at different locations of hiPSC-CM layers; Figure S6: electrical quantification of hiPSC-CMs; Figure S7: xy-inspections of diseased cell lines in monolayer configuration; Figure S8: electrical recordings of diseased cell lines; Figure S9: Local electrical response of CTRL and BRU hiPSC-CMs to isoproterenol; Table S1: mechanical methods comparison in quantifying single and layered CM contractility; and Table S2: electrical recording methods comparison of CM (PDF)

AUTHOR INFORMATION

Corresponding Authors

Michele Miragoli − *Laboratory of Applied Medical Technologies, Department of Medicine, University of Parma, 43126 Parma, Italy; Humanitas Research Hospital — IRCCS, 20089 Rozzano, Italy*; Email: michele.miragoli@unipr.it

Tomaso Zambelli − *Laboratory of Biosensors and Bioelectronics, Institute for Biomedical Engineering, ETH Zürich, 8092 Zürich, Switzerland*; orcid.org/0000-0003-0965-0950; Email: ztomaso@ethz.ch

Authors

Xinyu Zhang − *Laboratory of Biosensors and Bioelectronics, Institute for Biomedical Engineering, ETH Zürich, 8092 Zürich, Switzerland*; orcid.org/0000-0002-7762-0991

Margherita Burattini − *Laboratory of Applied Medical Technologies, Department of Medicine, University of Parma, 43126 Parma, Italy; Department of Maternity, Surgery and Dentistry, University of Verona, 37134 Verona, Italy*; orcid.org/0000-0002-6899-5791

Jens Duru − *Laboratory of Biosensors and Bioelectronics, Institute for Biomedical Engineering, ETH Zürich, 8092 Zürich, Switzerland*

Nafsika Chala − *Laboratory of Thermodynamics in Emerging Technologies, Department of Mechanical and Process Engineering, ETH Zürich, 8092 Zurich, Switzerland*; orcid.org/0000-0002-2293-6585

Nino Wyssen − *Laboratory of Biosensors and Bioelectronics, Institute for Biomedical Engineering, ETH Zürich, 8092 Zürich, Switzerland*

"Carla Cofino Fabres − *Department of Applied Stem Cell Technologies, TechMed Centre, University of Twente, 7500 AE Enschede, The Netherland*

Jose Manuel Rivera Arbelaez − *Department of Applied Stem Cell Technologies, TechMed Centre, University of Twente, 7500 AE Enschede, The Netherland*; orcid.org/0000-0002-0075-6006

Robert Passier − *Department of Applied Stem Cell Technologies, TechMed Centre, University of Twente, 7500 AE Enschede, The Netherland*

Dimos Poulikakos − *Laboratory of Thermodynamics in Emerging Technologies, Department of Mechanical and Process Engineering, ETH Zürich, 8092 Zurich, Switzerland*; orcid.org/0000-0001-5733-6478

Aldo Ferrari − *Laboratory of Thermodynamics in Emerging Technologies, Department of Mechanical and Process Engineering, ETH Zürich, 8092 Zurich, Switzerland; Experimental Continuum Mechanics, EMPA, Swiss Federal Laboratories for Material Science and Technologies, 8600 Dübendorf, Switzerland*

Christina Tringides − *Laboratory of Biosensors and Bioelectronics, Institute for Biomedical Engineering, ETH Zürich, 8092 Zürich, Switzerland*

https://doi.org/10.1021/acsnano.4c03896
ACS Nano XXXX, XXX, XXX−XXX

János Vörös − *Laboratory of Biosensors and Bioelectronics, Institute for Biomedical Engineering, ETH Zürich, 8092 Zürich, Switzerland;* orcid.org/0000-0001-6054-6230
Giovanni Battista Luciani − *Department of Maternity, Surgery and Dentistry, University of Verona, 37134 Verona, Italy*

Complete contact information is available at: https://pubs.acs.org/10.1021/acsnano.4c03896

Notes

The authors declare no competing financial interest.

ACKNOWLEDGMENTS

X.Z. was supported by the EU H2020 Marie Skłodowska-Curie Action (ITN "SENTINEL" no. 812398 to T.Z.). M.B. was supported by the Scientific Exchange Grants program of the European Molecular Biology Organization (EMBO, grant no. 10207). J.D. was supported by the Swiss National Science Foundation (SNSF no. 182779 to J.V.). M.M. was supported by the University of Parma through the action "BANDO YIRG UNIPR" co-funded by MUR-Italian Ministry of Universities and Research - D.M. 737/2021 and by PNR - PNRR − NextGenerationEU and National Recovery and Resilience Plan (NRRP), Mission 4 Component 2 Investment 1.5 - Call for tender No.3277 of 30/12/2021 of Italian Ministry of University and Research funded by the European Union − NextGenerationEU (no. ECS00000033, Ecosister) and "FIL-Quota Incentivante" of University of Parma and cosponsored by Fondazione Cariparma.

REFERENCES

(1) Roth, G. A.; Mensah, G. A.; Johnson, C. O. Global Burden of Cardiovascular Diseases and Risk Factors, 1990−2019. *J. Am. Coll. Cardiol.* **2020**, *76*, 2982−3021.
(2) Vagnozzi, R. J.; Molkentin, J. D.; Houser, S. R. New Myocyte Formation in the Adult Heart. *Circ. Res.* **2018**, *123*, 159−176.
(3) Vuorenpää, H.; Björninen, M.; Välimäki, H.; Ahola, A.; Kroon, M.; Honkamäki, L.; Koivumäki, J. T.; Pekkanen-Mattila, M. Building blocks of microphysiological system to model physiology and pathophysiology of human heart. *Front. Physiol.* **2023**, *14*, No. 1213959.
(4) Quinn, T. A.; Kohl, P. Cardiac Mechano-Electric Coupling: Acute Effects of Mechanical Stimulation on Heart Rate and Rhythm. *Physiol. Rev.* **2021**, *101*, 37−92.
(5) Bers, D. M. Cardiac excitation-contraction coupling. *Nature* **2002**, *415*, 198−205.
(6) Rohr, S.; Kucera, J. P.; Fast, V. G.; Kléber, A. G. Paradoxical Improvement of Impulse Conduction in Cardiac Tissue by Partial Cellular Uncoupling. *Science* **1997**, *275*, 841−844.
(7) Li, K. H. C.; Lee, S.; Yin, C.; Liu, T.; Ngarmukos, T.; Conte, G.; Yan, G.-X.; Sy, R. W.; Letsas, K. P.; Tse, G. Brugada syndrome: A comprehensive review of pathophysiological mechanisms and risk stratification strategies. *IJC Heart & Vasculature* **2020**, *26*, No. 100468.
(8) Tse, G.; Liu, T.; Li, K. H. C.; Laxton, V.; Chan, Y. W. F.; Keung, W.; Li, R. A.; Yan, B. P. Electrophysiological Mechanisms of Brugada Syndrome: Insights from Pre-clinical and Clinical Studies. *Front. Physiol.* **2016**, *7*, 467.
(9) Clippinger, S. R.; Cloonan, P. E.; Greenberg, L.; Ernst, M.; Stump, W. T.; Greenberg, M. J. Disrupted mechanobiology links the molecular and cellular phenotypes in familial dilated cardiomyopathy. *Proc. Natl. Acad. Sci. U. S. A.* **2019**, *116*, 17831−17840.
(10) McNally, E. M.; Mestroni, L. Dilated Cardiomyopathy. *Circ. Res.* **2017**, *121*, 731−748.
(11) Damluji, A. A.; van Diepen, S.; Katz, J. N.; Menon, V.; Tamis-Holland, J. E.; Bakitas, M.; Cohen, M. G.; Balsam, L. B.; Chikwe, J.; American Heart Association Council on Clinical Cardiology; Council on Arteriosclerosis, Thrombosis and Vascular Biology; Council on Cardiovascular Surgery and Anesthesia; Council on Cardiovascular and Stroke Nursing. Mechanical Complications of Acute Myocardial Infarction: A Scientific Statement From the American Heart Association. *Circulation* **2021**, *144*, e16−e35.
(12) Jia, B. Z.; Qi, Y.; Wong-Campos, J. D.; Megason, S. G.; Cohen, A. E. A bioelectrical phase transition patterns the first vertebrate heartbeats. *Nature* **2023**, *622*, 149−155.
(13) Losurdo, P.; Stolfo, D.; Merlo, M.; Barbati, G.; Gobbo, M.; Gigli, M.; Ramani, F.; Pinamonti, B.; Zecchin, M.; Finocchiaro, G.; Mestroni, L.; Sinagra, G. Early Arrhythmic Events in Idiopathic Dilated Cardiomyopathy. *JACC: Clinical Electrophysiology* **2016**, *2*, 535−543.
(14) Rohr, S. Role of gap junctions in the propagation of the cardiac action potential. *Cardiovasc. Res.* **2004**, *62*, 309−322.
(15) Sheehy, S. P.; Grosberg, A.; Parker, K. K. The contribution of cellular mechanotransduction to cardiomyocyte form and function. *Biomechanics and Modeling in Mechanobiology* **2012**, *11*, 1227−1239.
(16) Kucera, J. P.; Rohr, S.; Rudy, Y. Localization of sodium channels in intercalated disks modulates cardiac conduction. *Circ. Res.* **2002**, *91*, 1176−1182.
(17) Adams, W. P.; et al. Extracellular Perinexal Separation Is a Principal Determinant of Cardiac Conduction. *Circ. Res.* **2023**, *133*, 658−673.
(18) Schultz, F.; Swiatlowska, P.; Alvarez-Laviada, A.; Sanchez-Alonso, J. L.; Song, Q.; de Vries, A. A. F.; Pijnappels, D. A.; Ongstad, E.; Braga, V. M. M.; Entcheva, E.; Gourdie, R. G.; Miragoli, M.; Gorelik, J. Cardiomyocyte−myofibroblast contact dynamism is modulated by connexin-43. *FASEB J.* **2019**, *33*, 10453−10468.
(19) Liu, Z.; Tan, J. L.; Cohen, D. M.; Yang, M. T.; Sniadecki, N. J.; Ruiz, S. A.; Nelson, C. M.; Chen, C. S. Mechanical tugging force regulates the size of cell−cell junctions. *Proc. Natl. Acad. Sci. U. S. A.* **2010**, *107*, 9944−9949.
(20) Wang, N.; Butler, J. P.; Ingber, D. E. Mechanotransduction Across the Cell Surface and Through the Cytoskeleton. *Science* **1993**, *260*, 1124−1127.
(21) Samarel, A. M. Costameres, focal adhesions, and cardiomyocyte mechanotransduction. *American Journal of Physiology-Heart and Circulatory Physiology* **2005**, *289*, H2291.
(22) Yang, X.; Pabon, L.; Murry, C. E. Engineering Adolescence. *Circ. Res.* **2014**, *114*, 511−523.
(23) Devalla, H. D.; Passier, R. Cardiac differentiation of pluripotent stem cells and implications for modeling the heart in health and disease. *Sci. Transl. Med.* **2018**, *10*, No. eaah5457.
(24) Musunuru, K.; Sheikh, F.; Gupta, R. M.; Houser, S. R.; Maher, K. O.; Milan, D. J.; Terzic, A.; Wu, J. C.; American Heart Association Council on Functional Genomics and Translational Biology; Council on Cardiovascular Disease in the Young; Council on Cardiovascular and Stroke Nursing. Induced Pluripotent Stem Cells for Cardiovascular Disease Modeling and Precision Medicine: A Scientific Statement From the American Heart Association. *Circ. Gen. Precis. Med.* **2018**, *11*, No. e000043.
(25) Li, J.; Hua, Y.; Miyagawa, S.; Zhang, J.; Li, L.; Liu, L.; Sawa, Y. hiPSC-Derived Cardiac Tissue for Disease Modeling and Drug Discovery. *International Journal of Molecular Sciences* **2020**, *21*, 8893.
(26) Liang, P.; Lan, F.; Lee, A. S.; Gong, T.; Sanchez-Freire, V.; Wang, Y.; Diecke, S.; Sallam, K.; Knowles, J. W.; Wang, P. J.; Nguyen, P. K.; Bers, D. M.; Robbins, R. C.; Wu, J. C. Drug Screening Using a Library of Human Induced Pluripotent Stem Cell-Derived Cardiomyocytes Reveals Disease Specific Patterns of Cardiotoxicity. *Circulation* **2013**, *127*, 1677−1691.
(27) Dou, W.; Malhi, M.; Zhao, Q.; Wang, L.; Huang, Z.; Law, J.; Liu, N.; Simmons, C. A.; Maynes, J. T.; Sun, Y. Microengineered platforms for characterizing the contractile function of in vitro cardiac models. *Microsyst. Nanoeng.* **2022**, *8*, 26.

(28) Hayes, H. B.; Nicolini, A. M.; Arrowood, C. A.; Chvatal, S. A.; Wolfson, D. W.; Cho, H. C.; Sullivan, D. D.; Chal, J.; Fermini, B.; Clements, M.; Ross, J. D.; Millard, D. C. Novel method for action potential measurements from intact cardiac monolayers with multiwell microelectrode array technology. *Sci. Rep.* **2019**, *9*, 11893.
(29) Gao, J.; Liao, C.; Liu, S.; Xia, T.; Jiang, G. Nanotechnology: new opportunities for the development of patch-clamps. *J. Nanobiotechnol.* **2021**, *19*, 97.
(30) Dunlop, J.; Bowlby, M.; Peri, R.; Vasilyev, D.; Arias, R. High-throughput electrophysiology: an emerging paradigm for ion-channel screening and physiology. *Nat. Rev. Drug Discovery* **2008**, *7*, 358−368.
(31) Obien, M. E. J.; Deligkaris, K.; Bullmann, T.; Bakkum, D. J.; Frey, U. Revealing neuronal function through microelectrode array recordings. *Front. Neurosci.* **2015**, *8*, 423.
(32) Ballini, M.; et al. A 1024-Channel CMOS Microelectrode Array With 26,400 Electrodes for Recording and Stimulation of Electrogenic Cells In Vitro. *IEEE journal of solid-state circuits* **2014**, *49*, 2705−2719.
(33) Dragas, J.; Viswam, V.; Shadmani, A.; Chen, Y.; Bounik, R.; Stettler, A.; Radivojevic, M.; Geissler, S.; Obien, M.; Müller, J.; Hierlemann, A. A Multi-Functional Microelectrode Array Featuring 59760 Electrodes, 2048 Electrophysiology Channels, Stimulation, Impedance Measurement and Neurotransmitter Detection Channels. *IEEE journal of solid-state circuits* **2017**, *52*, 1576−1590.
(34) Lee, J.; Gänswein, T.; Ulusan, H.; Emmenegger, V.; Saguner, A. M.; Duru, F.; Hierlemann, A. Repeated and On-Demand Intracellular Recordings of Cardiomyocytes Derived from Human-Induced Pluripotent Stem Cells. *ACS Sensors* **2022**, *7*, 3181−3191.
(35) Ferrari, A. Recent technological advancements in traction force microscopy. *Biophysical Reviews* **2019**, *11*, 679−681.
(36) Sabass, B.; Gardel, M. L.; Waterman, C. M.; Schwarz, U. S. High Resolution Traction Force Microscopy Based on Experimental and Computational Advances. *Biophys. J.* **2008**, *94*, 207−220.
(37) Colin-York, H.; Shrestha, D.; Felce, J. H.; Waithe, D.; Moeendarbary, E.; Davis, S. J.; Eggeling, C.; Fritzsche, M. Super-Resolved Traction Force Microscopy (STFM). *Nano Lett.* **2016**, *16*, 2633−2638.
(38) Laurila, E.; Ahola, A.; Hyttinen, J.; Aalto-Setälä, K. Methods for in vitro functional analysis of iPSC derived cardiomyocytes — Special focus on analyzing the mechanical beating behavior. *Biochimica et Biophysica Acta (BBA) - Molecular Cell Research* **2016**, *1863*, 1864−1872.
(39) Huang, Y.; Schell, C.; Huber, T. B.; Şimşek, A. N.; Hersch, N.; Merkel, R.; Gompper, G.; Sabass, B. Traction force microscopy with optimized regularization and automated Bayesian parameter selection for comparing cells. *Sci. Rep.* **2019**, *9*, 539.
(40) Ribeiro, M. C.; Tertoolen, L. G.; Guadix, J. A.; Bellin, M.; Kosmidis, G.; D'Aniello, C.; Monshouwer-Kloots, J.; Goumans, M.-J.; Wang, Y.-l.; Feinberg, A. W.; Mummery, C. L.; Passier, R. Functional maturation of human pluripotent stem cell derived cardiomyocytes in vitro − Correlation between contraction force and electrophysiology. *Biomaterials* **2015**, *51*, 138−150.
(41) Czirok, A.; Isai, D. G.; Kosa, E.; Rajasingh, S.; Kinsey, W.; Neufeld, Z.; Rajasingh, J. Optical-flow based non-invasive analysis of cardiomyocyte contractility. *Sci. Rep.* **2017**, *7*, 10404.
(42) Sala, L.; et al. Musclemotion: A Versatile Open Software Tool to Quantify Cardiomyocyte and CardiacMuscle Contraction In Vitro and In Vivo. *Circ. Res.* **2018**, *122*, e5−e16.
(43) Frotscher, R.; Muanghong, D.; Dursun, G.; Goßmann, M.; Temiz-Artmann, A.; Staat, M. Sample-specific adaption of an improved electro-mechanical model of in vitro cardiac tissue. *J. Biomech.* **2016**, *49*, 2428−2435.
(44) McCain, M. L.; Agarwal, A.; Nesmith, H. W.; Nesmith, A. P.; Parker, K. K. Micromolded gelatin hydrogels for extended culture of engineered cardiac tissues. *Biomaterials* **2014**, *35*, 5462−5471.
(45) Bergert, M.; Lendenmann, T.; Zündel, M.; Ehret, A. E.; Panozzo, D.; Richner, P.; Kim, D. K.; Kress, S. J. P.; Norris, D. J.; Sorkine-Hornung, O.; Mazza, E.; Poulikakos, D.; Ferrari, A. Confocal reference free traction force microscopy. *Nat. Commun.* **2016**, *7*, No. 12814.
(46) Meister, A.; Gabi, M.; Behr, P.; Studer, P.; Vörös, J.; Niedermann, P.; Bitterli, J.; Polesel-Maris, J.; Liley, M.; Heinzelmann, H.; Zambelli, T. FluidFM: Combining Atomic Force Microscopy and Nanofluidics in a Universal Liquid Delivery System for Single Cell Applications and Beyond. *Nano Lett.* **2009**, *9*, 2501−2507.
(47) Li, M.; Liu, L.; Zambelli, T. FluidFM for single-cell biophysics. *Nano Research* **2022**, *15*, 773−786.
(48) Kress, S. J. P.; Antolinez, F. V.; Richner, P.; Jayanti, S. V.; Kim, D. K.; Prins, F.; Riedinger, A.; Fischer, M. P. C.; Meyer, S.; McPeak, K. M.; Poulikakos, D.; Norris, D. J. Wedge Waveguides and Resonators for Quantum Plasmonics. *Nano Lett.* **2015**, *15*, 6267−6275.
(49) Nguyen, D. T.; Nagarajan, N.; Zorlutuna, P. Effect of Substrate Stiffness on Mechanical Coupling and Force Propagation at the Infarct Boundary. *Biophys. J.* **2018**, *115*, 1966−1980.
(50) Pfeiffer, E. R.; Tangney, J. R.; Omens, J. H.; McCulloch, A. D. Biomechanics of Cardiac Electromechanical Coupling and Mechano-electric Feedback. *J. Biomech. Eng.* **2014**, *136*, No. 021007.
(51) Lendenmann, T.; Schneider, T.; Dumas, J.; Tarini, M.; Giampietro, C.; Bajpai, A.; Chen, W.; Gerber, J.; Poulikakos, D.; Ferrari, A.; Panozzo, D. Cellogram: On-the-Fly Traction Force Microscopy. *Nano Lett.* **2019**, *19*, 6742−6750.
(52) Lucas, B. D.; Kanade, T. An iterative image registration technique with an application to stereo vision. *Proceedings of the 7th International Joint Conference on Artificial Intelligence* 1981, *2*, 674−679.
(53) Wu, H.; Sankaranarayanan, A. C.; Chellappa, R. Online Empirical Evaluation of Tracking Algorithms. *IEEE Trans. Pattern Anal. Mach. Intell.* **2010**, *32*, 1443−1458.
(54) Sharma, P.; Kokare, P. M.; Kolekar, M. H. *Recent Trends in Communication, Computing, and Electronics; Lecture Notes in Electrical Engineering*; Springer: Singapore, 2019; 323−331.
(55) Dembo, M.; Wang, Y.-L. Stresses at the Cell-to-Substrate Interface during Locomotion of Fibroblasts. *Biophys. J.* **1999**, *76*, 2307−2316.
(56) Schwarz, U. S.; Soiné, J. R. D Traction force microscopy on soft elastic substrates: A guide to recent computational advances. *Biochimica et Biophysica Acta (BBA) - Molecular Cell Research* **2015**, *1853*, 3095−3104.
(57) Oria, R.; Wiegand, T.; Escribano, J.; Elosegui-Artola, A.; Uriarte, J. J.; Moreno-Pulido, C.; Platzman, I.; Delcanale, P.; Albertazzi, L.; Navajas, D.; Trepat, X.; García-Aznar, J. M.; Cavalcanti-Adam, E. A.; Roca-Cusachs, P. Force loading explains spatial sensing of ligands by cells. *Nature* **2017**, *552*, 219−224.
(58) Ito, M.; Nomura, S.; Morita, H.; Komuro, I. Trends and Limitations in the Assessment of the Contractile Properties of Human Induced Pluripotent Stem Cell-Derived Cardiomyocytes From Patients With Dilated Cardiomyopathy. *Front. Cardiovasc. Med.* **2020**, *7*, 154.
(59) Stoppel, W. L.; Kaplan, D. L.; Black, L. D. Electrical and mechanical stimulation of cardiac cells and tissue constructs. *Adv. Drug Delivery Rev.* **2016**, *96*, 135−155.
(60) Tulloch, N. L.; Muskheli, V.; Razumova, M. V.; Korte, F. S.; Regnier, M.; Hauch, K. D.; Pabon, L.; Reinecke, H.; Murry, C. E. Growth of Engineered Human Myocardium With Mechanical Loading and Vascular Coculture. *Circ. Res.* **2011**, *109*, 47−59.
(61) Chala, N.; Zhang, X.; Zambelli, T.; Zhang, Z.; Schneider, T.; Panozzo, D.; Poulikakos, D.; Ferrari, A. 4D Force Detection of Cell Adhesion and Contractility. *Nano Lett.* **2023**, *23*, 2467−2475.
(62) Liu, J.; Sun, N.; Bruce, M. A.; Wu, J. C.; Butte, M. J.; Muller, D. J. Atomic Force Mechanobiology of Pluripotent Stem Cell-Derived Cardiomyocytes. *PLoS One* **2012**, *7*, No. e37559.
(63) Yasuda, K. Dominant rule of community effect in synchronized beating behavior of cardiomyocyte networks. *Biophysical Reviews* **2020**, *12*, 481−501.
(64) Asai, Y.; Tada, M.; Otsuji, T. G.; Nakatsuji, N. Combination of functional cardiomyocytes derived from human stem cells and a highly-efficient microelectrode array system: an ideal hybrid model

https://doi.org/10.1021/acsnano.4c03896
ACS Nano XXXX, XXX, XXX−XXX

assay for drug development. *Curr. Stem Cell Res. Ther.* **2010**, *5*, 227–232.
(65) Duru, J.; Küchler, J.; Ihle, S. J.; Forró, C.; Bernardi, A.; Girardin, S.; Hengsteler, J.; Wheeler, S.; Vörös, J.; Ruff, T. Engineered Biological Neural Networks on High Density CMOS Microelectrode Arrays. *Frontiers in Neuroscience* **2022**, *16*, No. 829884.
(66) Bouten, C. V.; Cheng, C.; Vermue, I. M.; Gawlitta, D.; Passier, R. Cardiovascular Tissue Engineering and Regeneration: A Plead for Further Knowledge Convergence. *Tissue Engineering Part A* **2022**, *28*, 525–541.
(67) Reyes Lua, A. M.; Hopf, R.; Mazza, E. Factors influencing the mechanical properties of soft elastomer substrates for traction force microscopy. *Mech. Soft Mater.* **2020**, *2*, 6.
(68) Wells, S. P.; Waddell, H. M.; Sim, C. B.; Lim, S. Y.; Bernasochi, G. B.; Pavlovic, D.; Kirchhof, P.; Porrello, E. R.; Delbridge, L. M. D.; Bell, J. R. Cardiomyocyte functional screening: interrogating comparative electrophysiology of high-throughput model cell systems. *American Journal of Physiology-Cell Physiology* **2019**, *317*, C1256–C1267.
(69) Fang, J.; Wei, X.; Li, H.; Hu, N.; Liu, X.; Xu, D.; Zhang, T.; Wan, H.; Wang, P.; Xie, X. Cardiomyocyte electrical-mechanical synchronized model for high-content, dose-quantitative and time-dependent drug assessment. *Microsyst. Nanoeng.* **2021**, *7*, 26.
(70) Liu, W.; Han, J. L.; Tomek, J.; Bub, G.; Entcheva, E. Simultaneous Widefield Voltage and Dye-Free Optical Mapping Quantifies Electromechanical Waves in Human Induced Pluripotent Stem Cell-Derived Cardiomyocytes. *ACS Photonics* **2023**, *10*, 1070–1083.
(71) Ross, S. A.; Wakeling, J. M. Muscle shortening velocity depends on tissue inertia and level of activation during submaximal contractions. *Biology Letters* **2016**, *12*, No. 20151041.
(72) Hall, C.; Gehmlich, K.; Denning, C.; Pavlovic, D. Complex Relationship Between Cardiac Fibroblasts and Cardiomyocytes in Health and Disease. *J. Am. Heart Assoc.* **2021**, *10*, No. e019338.
(73) Ribeiro, M. C.; Slaats, R. H.; Schwach, V.; Rivera-Arbelaez, J. M.; Tertoolen, L. G. J.; van Meer, B. J.; Molenaar, R.; Mummery, C. L.; Claessens, M. M. A. E.; Passier, R. A cardiomyocyte show of force: A fluorescent alpha-actinin reporter line sheds light on human cardiomyocyte contractility versus substrate stiffness. *Journal of Molecular and Cellular Cardiology* **2020**, *141*, 54–64.
(74) McCain, M. L.; Lee, H.; Aratyn-Schaus, Y.; Kléber, A. G.; Parker, K. K. Cooperative coupling of cell-matrix and cell–cell adhesions in cardiac muscle. *Proc. Natl. Acad. Sci. U. S. A.* **2012**, *109*, 9881–9886.
(75) Pires, R. H.; Shree, N.; Manu, E.; Guzniczak, E.; Otto, O. Cardiomyocyte mechanodynamics under conditions of actin remodelling. *Philosophical Transactions of the Royal Society B: Biological Sciences* **2019**, *374*, No. 20190081.
(76) Shah, K.; Seeley, S.; Schulz, C.; Fisher, J.; Gururaja Rao, S. Calcium Channels in the Heart: Disease States and Drugs. *Cells* **2022**, *11*, 943.
(77) de Boer, T.; van Rijen, H.; van der Heyden, M.; de Bakker, J.; van Veen, T. Adrenergic regulation of conduction velocity in cultures of immature cardiomyocytes. *Netherlands Heart Journal* **2008**, *16*, 106–109.
(78) Kim, J. J.; Yang, L.; Lin, B.; Zhu, X.; Sun, B.; Kaplan, A. D.; Bett, G. C.; Rasmusson, R. L.; London, B.; Salama, G. Mechanism of automaticity in cardiomyocytes derived from human induced pluripotent stem cells. *Journal of molecular and cellular cardiology* **2015**, *81*, 81–93.
(79) Wang, H.-W.; Yang, Z.-F.; Zhang, Y.; Yang, J.-M.; Liu, Y.-M.; Li, C.-Z Beta-receptor activation increases sodium current in guinea pig heart. *Acta Pharmacologica Sinica* **2009**, *30*, 1115–1122.
(80) Sheehy, S. P.; Grosberg, A.; Qin, P.; Behm, D. J.; Ferrier, J. P.; Eagleson, M. A.; Nesmith, A. P.; Krull, D.; Falls, J. G.; Campbell, P. H.; McCain, M. L.; Willette, R. N.; Hu, E.; Parker, K. K. Toward improved myocardial maturity in an organ-on-chip platform with immature cardiac myocytes. *Experimental Biology and Medicine* **2017**, *242*, 1643–1656.
(81) Ahmad, F. S.; Jin, Y.; Grassam-Rowe, A.; Zhou, Y.; Yuan, M.; Fan, X.; Zhou, R.; Mu-u-min, R.; O'Shea, C.; Ibrahim, A. M.; Hyder, W.; Aguib, Y.; Yacoub, M.; Pavlovic, D.; Zhang, Y.; Tan, X.; Lei, M.; Terrar, D. A.; et al. Generation of cardiomyocytes from human-induced pluripotent stem cells resembling atrial cells with ability to respond to adrenoceptor agonists. *Philos. Trans. R. Soc. Lond. Ser. B, Biol. Sci.* **2023**, *378*, No. 20220312.
(82) Ernst, P.; Bidwell, P. A.; Dora, M.; Thomas, D. D.; Kamdar, F. Cardiac calcium regulation in human induced pluripotent stem cell cardiomyocytes: Implications for disease modeling and maturation. *Frontiers in Cell and Developmental Biology* **2023**, *10*, No. 986107.
(83) Antzelevitch, C.; et al. Loss-of-Function Mutations in the Cardiac Calcium Channel Underlie a New Clinical Entity Characterized by ST-Segment Elevation, Short QT Intervals, and Sudden Cardiac Death. *Circulation* **2007**, *115*, 442–449.
(84) Westhoff, M.; Dixon, R. E. Mechanisms and Regulation of Cardiac CaV1.2 Trafficking. *International Journal of Molecular Sciences* **2021**, *22*, 5927.
(85) Sader, J. E.; Sanelli, J. A.; Adamson, B. D.; Monty, J. P.; Wei, X.; Crawford, S. A.; Friend, J. R.; Marusic, I.; Mulvaney, P.; Bieske, E. J. Spring constant calibration of atomic force microscope cantilevers of arbitrary shape. *Rev. Sci. Instrum.* **2012**, *83*, 103705.
(86) Helfricht, N.; Mark, A.; Dorwling-Carter, L.; Zambelli, T.; Papastavrou, G. Extending the limits of direct force measurements: colloidal probes from sub-micron particles. *Nanoscale* **2017**, *9*, 9491–9501.
(87) Bonyar, A.; Nagy, G.; Gunstheimer, H.; Fläschner, G.; Horvath, R. Hydrodynamic function and spring constant calibration of FluidFM micropipette cantilevers. *Microsyst. Nanoeng.* **2024**, *10*, 26.
(88) Sittl, S.; Helfricht, N.; Papastavrou, G. Contactless calibration of microchanneled AFM cantilevers for fluidic force microscopy. *VIEW* **2024**, *5*, No. 20230063.
(89) Duru, J.; Maurer, B.; Giles Doran, C.; Jelitto, R.; Küchler, J.; Ihle, S. J.; Ruff, T.; John, R.; Genocchi, B.; Vörös, J. Investigation of the input-output relationship of engineered neural networks using high-density microelectrode arrays. *Biosens. Bioelectron.* **2023**, *239*, No. 115591.

https://doi.org/10.1021/acsnano.4c03896
ACS Nano XXXX, XXX, XXX–XXX